

## Genetic relationship between greisenization and Sn–W mineralization in vein and greisen deposits: Insights from the Panasqueira deposit (Portugal)

Gaëtan Launay<sup>1,\*</sup>, Stanislas Sizaret<sup>2</sup>, Philippe Lach<sup>3</sup>, Jérémie Melleton<sup>3</sup>, Eric Gloaguen<sup>2,3</sup> and Marc Poujol<sup>4</sup>

<sup>1</sup> Department of Earth Sciences, Laurentian University, Sudbury, Ontario P3E 2C6, Canada

<sup>2</sup> ISTO, UMR7327, Université d'Orléans, CNRS, BRGM, F-45071 Orléans, France

<sup>3</sup> BRGM, F-45060 Orléans, France

<sup>4</sup> Univ. Rennes, CNRS, Géosciences Rennes UMR, CNRS 6118, F-35000 Rennes, France

Received: 7 October 2020 / Accepted: 16 December 2020 / Publishing online: 23 February 2021

**Abstract** – The W–Sn Panasqueira ore deposit is a magmatic-hydrothermal system, which includes a high-grade quartz-vein type mineralization and a disseminated greisen-type mineralization occurring in the upper part of the Panasqueira two-mica granite. We investigated the genetic and chronological relationships between the greisenization of the Panasqueira granite and the formation of ore-bearing quartz veins by monitoring major and trace elements variations in quartz-white mica assemblages composing the two-mica granite, greisen and W–Sn-bearing quartz veins. The greisen is characterized by an overall depletion in Mg, Ti, Ca, Na, Ba, Sr, REE and enrichment in Fe, Li, Rb, Cs, Sn, W which reflect the breakdown of feldspars and fluid-rock interactions with W–Sn-bearing fluids. White-mica from greisen and mineralized quartz veins are enriched in granophile elements (F, Rb, Cs, Li, Sn, W and Zn) compared to magmatic muscovite from the two-mica granite. Trace elements contents in quartz depict trends which show the progressive enrichment in Ge and B and depletion in Al, Ti and Li from magmatic to hydrothermal quartz that emphasize the progressive evolution and cooling of the magmatic-hydrothermal system of Panasqueira. Geochemical similarities between quartz-white mica assemblages from greisen and wolframite-bearing veins suggest that greisenization and the formation of mineralized veins result from the same hydrothermal event and derived from the same source of hydrothermal fluids. Apatite from greisen and quartz vein yielded U–Pb ages of  $292 \pm 10$  Ma and  $295 \pm 5$  Ma respectively confirming that greisenization and the formation of mineralized veins occurred roughly at the same time. These ages also overlap with the emplacement age of the Panasqueira granite ( $296 \pm 4$  Ma), indicating a temporal link between greisenization, W–Sn mineralization and granite crystallization. Temperatures of the magmatic-hydrothermal system constrained by Ti-in quartz thermometry depicts a cooling trend from magmatic quartz of granite (700–600 °C) to hydrothermal quartz of greisen (500–400 °C) and veins (450–350 °C). These results suggest that greisenization and the formation of W–Sn bearing quartz veins occurred at the magmatic-hydrothermal transition, during which orthomagmatic fluids rich in volatils, incompatible elements and W–Sn were exsolved during the final solidification stage of the Panasqueira two-mica granite.

**Keywords:** vein and greisen Sn–W deposits / Panasqueira / white-mica chemistry / quartz trace chemistry / U–Pb dating of apatite / magmatic-hydrothermal evolution

\*Corresponding author: [glaunay@laurentian.ca](mailto:glaunay@laurentian.ca)

## 1 Introduction

Vein and greisen deposits supply an important source of tin–tungsten (Sn–W) (Kotlyar *et al.*, 1995; Robb, 2005; Werner *et al.*, 2014). This style of deposit is generally developed at the edge of granite cupolas that constitute the apical parts of larger polyphased granite intrusions (Stemprok, 1987; Pollard *et al.*, 1988; Lehmann, 1990; Pirajno, 1992; Černý *et al.*, 2005; Stemprok *et al.*, 2005). The formation of these deposits involves continuum of magmatic-hydrothermal processes with the circulation and the focusing of a large amount of mineralizing fluids (Pirajno, 1992; Černý *et al.*, 2005; Dolejš, 2015). These systems generally include (i) a disseminated mineralization within a massive greisen characterized by low grade and high tonnage and (ii) W–Sn bearing mineralized quartz veins usually characterized by high grade and low tonnage (Taylor, 1979; Taylor and Pollard, 1988; Lehmann, 1990; Mlynarczyk *et al.*, 2002).

It is well established that greisenization is caused by interactions between granite and hot acidic fluids (250 to 450 °C) released during the final crystallization stage of granite intrusions (Stemprok, 1987; Taylor and Pollard, 1988; Bishop, 1989; Pirajno, 2009). Based on structural, geochemical and geochronological data, numerous studies concluded that the formation of greisen and Sn–W-bearing veins are contemporaneous and result of the circulation of a single Sn–W-rich orthomagmatic fluid (with possible local evolution or mixing with other source(s) of fluids) (Stemprok, 1987; Halter *et al.*, 1996; Williamson *et al.*, 1997; Yokart *et al.*, 2003; Pirajno, 2009; Mao *et al.*, 2013; Zhao *et al.*, 2017; Korges *et al.*, 2018; Monnier *et al.*, 2018, 2020; Zheng *et al.*, 2018; Chen *et al.*, 2019).

Panasqueira is an historic world-class tungsten vein and greisen deposit characterized by a well-preserved magmatic-hydrothermal plumbing system. This deposit is one of the best-documented and characterized in the world and represents a reference site for the study of hydrothermal mechanisms leading to the formation of giant Sn–W ore deposits (Thadeu, 1951; Kelly and Rye, 1979; Polya, 1989; Polya *et al.*, 2000; Foxford *et al.*, 2000; Lecumberri-Sanchez *et al.*, 2017; Carocci *et al.*, 2018, 2020; Codeço *et al.*, 2017, 2019, 2020; Launay *et al.*, 2018; Launay, 2019; Mateus *et al.*, 2020; Martins *et al.*, 2020; Marignac *et al.*, 2020). Although most of these studies promote a genetic model involving the exsolution of an orthomagmatic fluid causing both the greisen alteration and the formation of wolframite-bearing veins (Kelly and Rye, 1979; Polya, 1989; Polya *et al.*, 2000; Lecumberri-Sanchez *et al.*, 2017; Codeço *et al.*, 2017, 2019, 2020; Launay *et al.*, 2018; Launay, 2019), a recent study (Carocci *et al.*, 2020) focused on the trace elements composition of tourmaline and rutile questions this genetic link and the origin of W–Sn-bearing fluids. Despite the absence of clear evidence, Carocci *et al.* (2020) proposed a new genetic model involving mixing between shallow meteoric/metamorphic fluids and W-bearing metamorphic fluids produced by biotite dehydration reactions in the deep crust (~20 km).

Quartz-mica assemblages are common both in greisen and in their associated mineralized veins, *e.g.* Panasqueira, Portugal (Kelly and Rye, 1979; Neiva, 1987; Neiva *et al.*, 2007), Piaotang, China (Legros *et al.*, 2016, 2018), Cínovec, Erzgebirge (Breiter *et al.*, 2017a, 2017b, 2019;

Müller *et al.*, 2018), Cligga Head, Cornwall (Sanderson *et al.*, 2008) and Echassières district, France (Monnier *et al.*, 2018, 2019). These minerals are able to incorporate a wide range of trace elements that can be used as indicators of the evolution of magmatic-hydrothermal systems (Miller *et al.*, 1981; Speer, 1984; Monier *et al.*, 1984; Neiva, 1987; Tischendorf *et al.*, 1997; Gomes and Neiva, 2000; Legros *et al.*, 2016, 2018; Breiter *et al.*, 2017a, 2017b; Müller *et al.*, 2018; Michaud *et al.*, 2020). The incorporation of elements in mica is controlled by the crystallization temperature (Monnier and Robert, 1986), the oxygen fugacity (Pichavant *et al.*, 2016) and their abundance in the source melt-fluids. Thereby, compositional variations in mica composing magmatic-hydrothermal systems is commonly used to (i) decipher signatures and source(s) of fluids and (ii) magmatic and hydrothermal mechanisms involved in the formation of ore deposits (Alfonso *et al.*, 2003; Hulsbosch *et al.*, 2014; Dostal *et al.*, 2015; Legros *et al.*, 2016, 2018; Breiter *et al.*, 2017a, 2017b, 2019; Van Daele *et al.*, 2018; Kaeter *et al.*, 2018).

Quartz is universally present in both hydrothermal and felsic magmatic environments. It is relatively resistant to post-crystallization alteration and able to incorporate a wide range of trace elements that can be used as a genetic pathfinder to track magmatic and hydrothermal processes (Monecke *et al.*, 2002; Götze *et al.*, 2004; Breiter *et al.*, 2017a, 2017b; Monnier *et al.*, 2018; Müller *et al.*, 2018). The concentrations of these trace elements are generally controlled by (i) their abundances in the parental melt and hydrothermal fluids, (ii) partitioning of these elements between co-genetic minerals and (iii) pressure and temperature conditions (Gurbanov *et al.*, 1999; Larsen *et al.*, 2004; Jacamon and Larsen, 2009; Thomas *et al.*, 2010). Recent studies have demonstrated that Ti content in quartz is generally correlated to the crystallization temperature (Thomas *et al.*, 2010; Huang and Audétat, 2012), while the evolution of Al, Ge and Li generally permit to highlight the melt differentiation induced by fractionated crystallization (Jacamon and Larsen, 2009). Trace element content in quartz is also commonly used to track the magmatic-hydrothermal processes in cases of deposits related to magmatic intrusions (Müller *et al.*, 2002; Breiter *et al.*, 2005, 2012; Rusk, 2012; Müller *et al.*, 2018; Monnier *et al.*, 2018). Recently, analyses of trace elements contents in quartz from the Beauvoir deposit demonstrated that greisenization and the formation of proximal Nb–Ta–Sn–W and distal Sb veins are related to the same hydrothermal fluid (Monnier *et al.*, 2018).

U–Pb dating of minerals occurring both in veins and greisen is another robust method to constrain temporal relationship between veins and greisen alteration. Based on U–Pb dating of cassiterite from greisen and W–Sn-bearing quartz veins of the Maopping deposit, Chen *et al.* (2019) proved that the formation of greisen and ore-bearing veins are coeval and highlighted that greisenization is a major mechanism for deposition of Sn–W mineralization.

In the following, we investigate the genetic and chronological relationships between greisenization and the formation of mineralized veins of the W–Sn Panasqueira ore deposit by applying the different analytical methods described above. Results of petrological and geochemical study with major and trace elements analyses in white-mica and quartz from the granite, greisen and ore-bearing quartz veins are

presented below. Signatures of the different populations of quartz and white-mica are then deciphered using principal component analysis (PCA) that permits to constrain correlations and behaviours of elements in the magmatic-hydrothermal system of Panasqueira.

New U–Pb dating on magmatic and hydrothermal apatite grains constrain the timing between granite emplacement, greisenization and formation of the mineralized veins. Based on the analysis of these various results, composition and the origin of fluids responsible for greisenization and the formation of the W–Sn mineralized veins is discussed. Finally, a conceptual model describing the formation of greisen and W–Sn-bearing quartz veins during the magmatic-hydrothermal transition in Panasqueira is proposed.

## 2 Geology of the W–Sn–(Cu) Panasqueira deposit

### 2.1 Regional geology

The W–Sn Panasqueira ore deposit is located in the Central Iberian Zone (CIZ) that covers the middle part of the Iberian Variscan Belt (Julivert *et al.*, 1972) (Fig. 1a). This tectono-metamorphic zone is mainly composed of a thick (8–11 km) monotonous Neoproterozoic schisto-greywacke sequence, in which numerous granitic intrusions were emplaced during the latest stages of the Variscan orogeny (Dias *et al.*, 1998; Castro *et al.*, 2002; Villaseca *et al.*, 2014). The CIZ is particularly rich in Sn–W deposits and occurrences (Vilas *et al.*, 1990), whose formations are related to the emplacement of granitic intrusions. These deposits comprise mostly vein and greisen mineralized systems like Regoufe, Gois and Panasqueira, which were/are mainly mined for their W mineralization.

The W–Sn–(Cu) Panasqueira deposit is in Beira Baixa province located south of the Serra da Estrela granitic Massif. This region is underlain by Beira schist *i.e.* schist greywacke sequence affected upright, tight folding and by low-grade greenschist metamorphism related to the Variscan orogeny (Azor *et al.*, 2019). The presence of spotted schist delineates a thermal metamorphism aureole, which indicates the presence of a sub-outcropping granitic intrusion (Clark, 1964; Kelly and Rye, 1979; Bussink, 1984) (Fig. 1b). The surface distribution of spotted schist, drill holes which intersected the intrusion over the Panasqueira district as well as gravimetric survey show that this intrusion forms a laccolith elongated in the NW–SE direction ( $7.5 \times 4.5$  km) for a thickness less than 2 km (Thadeu, 1951; Clark, 1964; Kelly and Rye 1979; Hebblethwaite and Antao, 1982; Ribeiro, 2017). The granite's roof dips gently to the NE in the northeastern part and steeply to the SW in the southwestern part of the intrusion (Figs. 1b and 1c). Underground mining infrastructure (Figs. 1b and 1c) crosscut the greisenized apex of the granite. The economic W–Sn mineralization consists of a dense swarm of sub-horizontal quartz veins mostly hosted by the metasedimentary host rock.

### 2.2 Greisen of Panasqueira

In the drill hole SCB2, the granite intrusion of Panasqueira exhibits a progressive increase of alteration up to the granite-cupola (Fig. 1d) (Launay, 2019). The intrusion is a porphyritic

two-mica granite composed of K-feldspar phenocrysts, albite, muscovite, biotite and euhedral quartz phenocrysts (quartz eyes) (Figs. 1d and 2a). Accessory minerals include zircon, apatites and Fe–Ti oxides. In this deeper part, greisenization occurs locally as narrow alteration halos around fractures and mineralized veinlets (Fig. 1d) (Launay, 2019).

The upper part of the intrusion exhibits a thick massive greisen (up to 30 m in the drill hole SCB2) resulting from an intense fluid-rock interaction which affected the underlying two-mica granite (Figs. 1c and 1d). The cupola (Level 1 and Level 530 of the mine) and granitic aplites occurring at the top of the granite intrusion were also entirely converted into greisen and exhibit the same texture and mineral assemblage than the one observed in the drill hole SCB2. This greisen is marked by the total breakdown of feldspars and biotite, which were replaced by a medium- to coarse-grained quartz-white mica assemblage (Fig. 2b) (Bussink, 1984; Neiva, 1987; Launay, 2019). Euhedral quartz phenocrysts in the two-mica granite were partially preserved in the greisen during hydrothermal alteration (Fig. 2b). Apatite, rutile, cassiterite, scarce wolframite, columbo-tantalite and sulfides (chalcopyrite, sphalerite, pyrite and arsenopyrite) occur as accessory minerals disseminated in the greisen. Sulfides, cassiterite and scarce wolframite infilled vugs observed in greisen (Launay, 2019) and can be associated with euhedral quartz in vugs. Flat-dipping mineralized veins can be also observed within the greisen cupola (Fig. 2c). These veins, which crosscut the sharp contact between the cupola and the metasedimentary host rock (Fig. 2c), exhibit the same paragenesis (*i.e.* muscovite, quartz wolframite and sulfides) as the mineralized veins present in the metasedimentary host rocks. More photos displaying the characteristics of the greisen of Panasqueira are provided in supplementary material ESM1A.

### 2.3 The ore-bearing quartz veins

The W–Sn–(Cu) mineralization of Panasqueira is hosted by a dense network of low-dipping quartz veins crosscutting the vertical foliation planes of the metasedimentary rocks. This vein network defines an ore zone connected with the greisen cupola at depth (Figs. 1b and 1c). This ore zone extends over an area of about 6 km<sup>2</sup> for a depth extension reaching 500 m (Polya *et al.*, 2000; Wheeler, 2015). The veins have recorded a complex history involving different type of mineralization: an early W–Sn stage and a late sulfide (Cu) mineralization event. The complex paragenetic sequence of veins was described in detail by Kelly and Rye (1979) and by Foxford *et al.* (1991, 2000) and Polya *et al.* (2000). At least five mineralization stages are recognized in the veins: the Quartz-Tourmaline (QTS) stage, the Main Oxide Silicate Stage (MOSS), the Main Sulfide Stage (MSS), the Pyrrhotite Alteration Stage (PAS) and the Late Carbonate Stage (LCS). The two earliest mineralization stages (QTS and MOSS) constitute a continuous sequence, which was then superimposed and/or cross-cut by the late mineralization stages (MSS, PAS and LCS).

The (QTS) corresponds to an early precursor of the W–Sn mineralization (MOSS) and marks the earliest phase of the hydrothermal activity in the mineralized veins of Panasqueira (Codeço *et al.*, 2017; Launay *et al.*, 2018; Carocci *et al.*, 2018, 2020). This stage consists of an intense tourmalinization of the

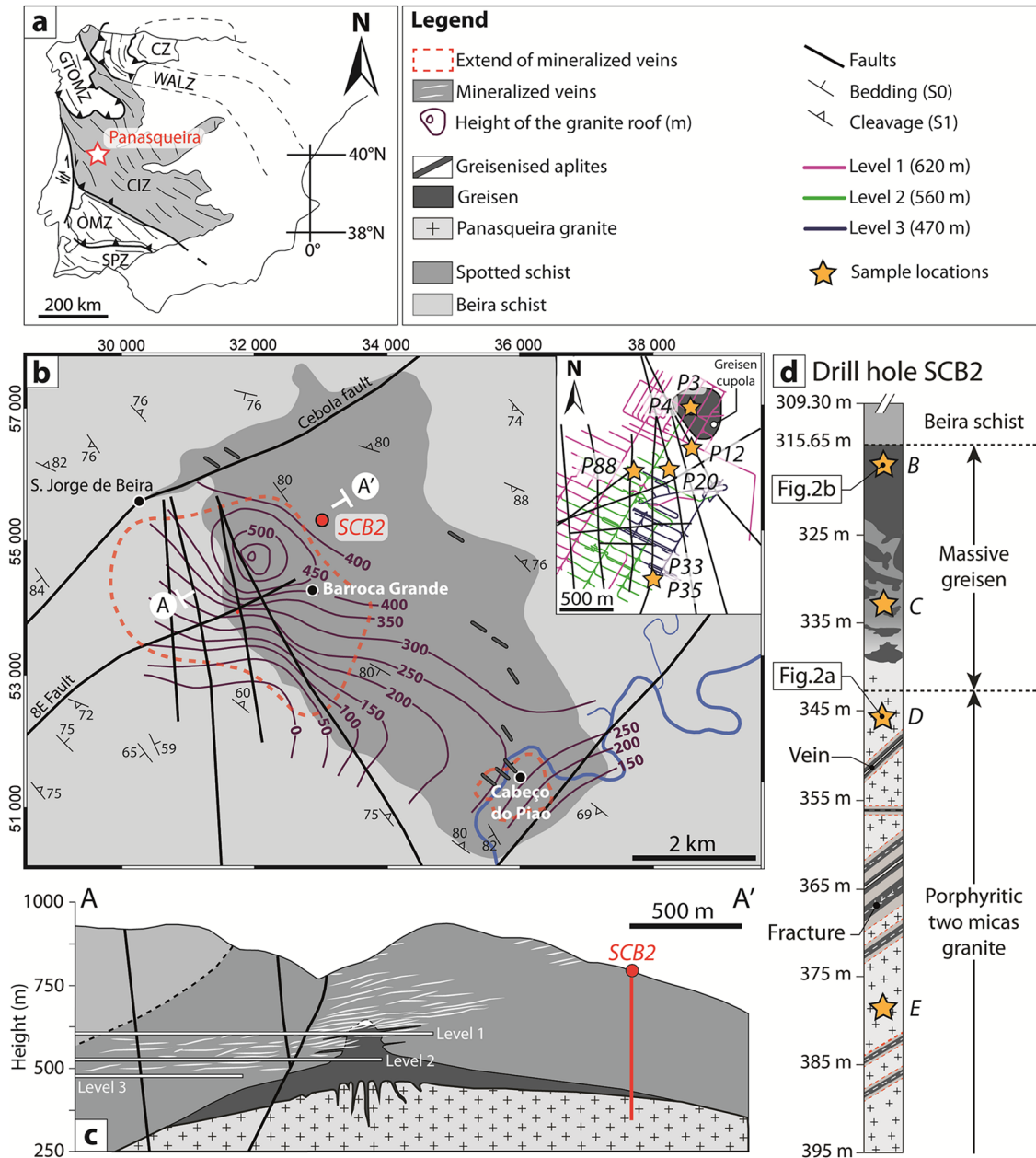


**Fig. 1.** (a) Tectono-metamorphic map of the Iberian Varican belt displaying location of the Panasqueira deposit (red star). CZ: Cantabrian Zone, WALZ: West Asturian-Leonese Zone, GTMZ: Galicia Trás-os-Montes Zone, CIZ: Central Iberian Zone, OMZ: Ossa-Morena Zone and SPZ: South Portuguese Zone (Julivert *et al.*, 1972) (b) Geological map of the Panasqueira district showing the lateral extent of the non-outcropping granite intrusion and the mineralized vein system (modified from Launay, 2019). Projected lat./lon. coordinates, ETRS89 TM6. (c) Geological cross section (A-A') displaying the relationship between greisen and the mineralized vein network. (d) Drill hole SCB2 displaying the vertical zoning of greisenization of the Panasqueira two mica granite (Location of the drill hole is displayed on the geological map and on the cross-section) (modified from Launay, 2019).

metasedimentary host rock and the opening of fibrous quartz-tourmaline veinlets (Fig. 2d). Tourmalines are commonly associated with white-mica, apatite, W-rich rutile (Carocci *et al.*, 2018, 2020) and, in some cases, with wolframite and cassiterite. The QTS is generally followed directly by the W-Sn mineralizing stage (MOSS).

The MOSS carries the W-Sn mineralization and constitutes the most volumetrically important stage ( $\approx 60\%$  of the

vein volume) (Kelly and Rye, 1979; Polyá *et al.*, 2000). The MOSS can be subdivided in two sub-stages:

- 1 An early event marked by the crystallization of quartz-white mica-apatite rich selvages along the schist vein contacts (Figs. 2e and 2f). This sub-stage is usually in direct continuity with tourmaline of the QTS. Cassiterite can be found within these selvages as intergrown with tourmaline and white-mica.

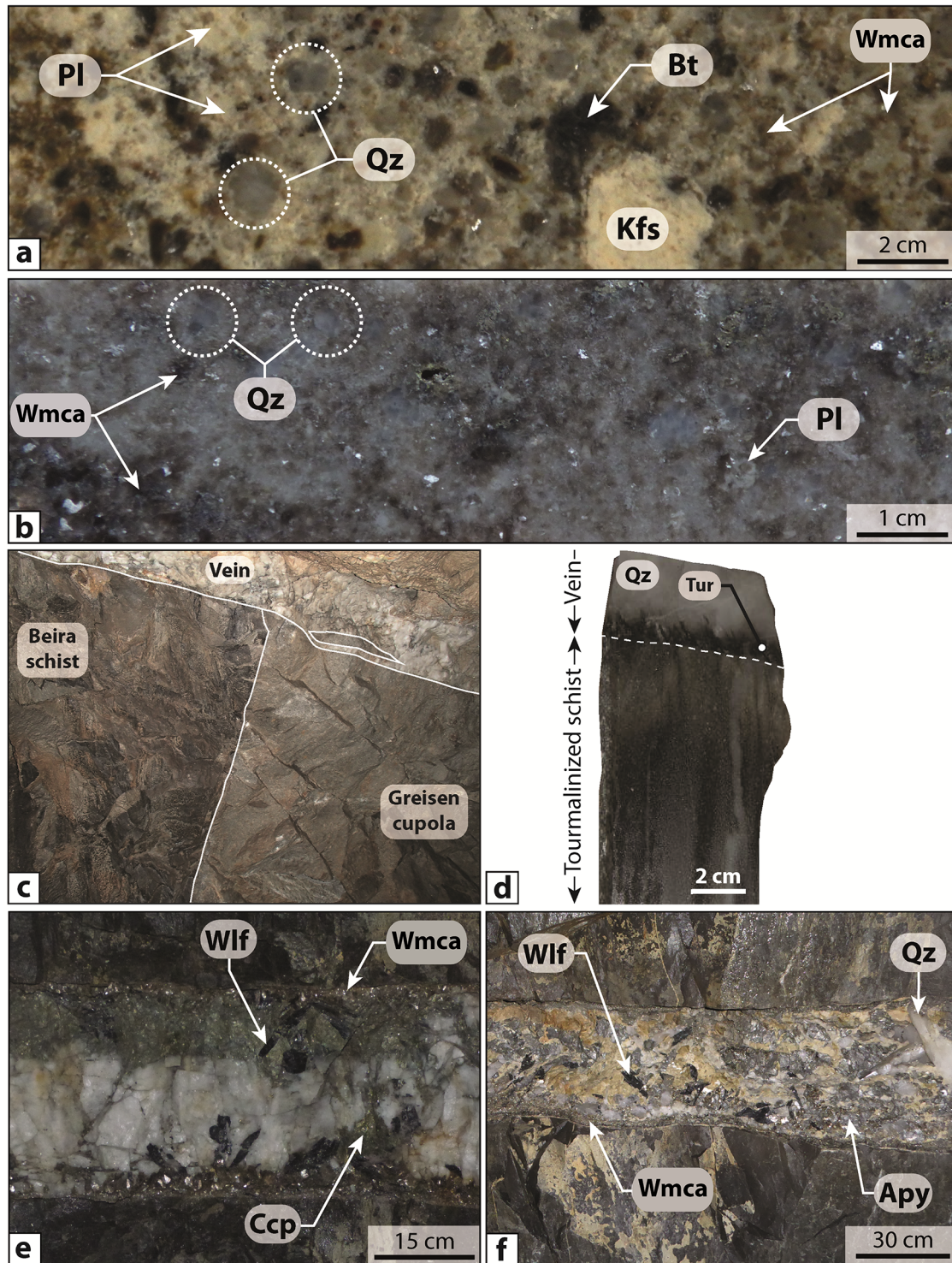


**Fig. 2.** Textural and mineralogical characteristics of (a) the Panasqueira two-mica granite and (b) greisen in the drill hole SCB2. (c) Contact between the greisen cupola and the metasedimentary host rock. A mineralized quartz vein crosscut this contact. (d) Quartz-tourmaline veinlet characteristic of the QTS mineralization stage. (e) Typical quartz-white mica vein with wolframite mineralization. White-mica forms fringes along the schist-vein contacts. (f) Geodic vein displaying euhedral quartz and wolframite nugget infilling vugs between quartz crystals. Note that vugs were also infilled by sulfphides and carbonates during the late mineralization stages. Abbreviations from [Whitney and Evans \(2010\)](#): Apy: Arsenopyrite; Bt: Biotite; Ccp: Chalcopyrite; Kfs: K-feldspar; Wmca: White-mica; Pl: Plagioclase; Qz: Quartz; Wlf: Wolframite.

2 The sequence continued with a typical syntaxial overgrowth of the vein selvages marked by the crystallization of large euhedral crystals of quartz (Fig. 2f). This quartz crystallized preferentially vertically and perpendicularly to the schist-vein contact. The veins exhibit geodic texture characterized by the presence of large void spaces between the crystals of quartz (Fig. 2f). The crystallization of quartz was followed by the cavity-filling with white-mica, apatite, cassiterite and wolframite which occurs as large nugget-like aggregates. More photos displaying the characteristics of the ore-bearing quartz veins of Panasqueira are provided in ESM1B.

### 3 Samples and methods

#### 3.1 Sampling

Quartz and white-mica are ubiquitous in the magmatic-hydrothermal system of Panasqueira. Samples of the Panasqueira two-mica granite and greisen were collected in the drill hole SCB2 and within the cupola (Level 1 in the mine). Samples of veins representative of the first mineralization stages (QTS and MOSS) were also collected in the mine. Ore-bearing quartz veins with rich-apatite selvage were also sampled to constrain the timing between the granite cooling, greisenization and the W-Sn mineralization stage by U–Pb dating of apatite. The locations of the samples used in this study are displayed in Figure 1.

#### 3.2 Scanning electron microscopy and cathodoluminescence imaging

Mineralogical and micro-textural characteristics of samples were examined on polished thin sections by optical microscopy (reflected and transmitted light) and by scanning electron microscopy (SEM) using a Merlin compact Zeiss high resolution scanning electronic microscope equipped with a Gemini I detector (BRGM, University of Orléans). To display chemical zoning present in some minerals (like mica and apatite), element mapping was performed by SEM using an acceleration voltage of 15 kV.

The cathodoluminescence (CL) images of quartz and apatite were collected at the BRGM (French Geological Survey) using a TESCAN MIRA 3 Scanning Electronic Microscope (SEM) equipped with a single channel panchromatic detector. This detector has a spectral range from 350 to 650 nm providing greyscale images of the CL emissivity. Polished thick and thin sections were examined for a working distance of 16 mm with an accelerating voltage of 20 kV and a current of 15 nA. For the textural analysis of quartz, the image acquisition has been performed with a scanning speed ranging from 100 to 500  $\mu\text{s}/\text{pixel}$  depending on the presence of highly luminescent minerals (apatite, carbonate) associated with quartz.

#### 3.3 Mineral chemistry

Major and minor elements compositions of white-mica were determined on polished thin sections using a Cameca SX-Five electron probe micro-analyzers (EPMA) at the Institut des

Sciences de la Terre d'Orléans. Analyses were performed using an accelerating voltage of 15 kV, an electron beam current of 6 nA and a beam diameter of 2  $\mu\text{m}$ . Elemental mapping of white-mica have been performed using an accelerating voltage of 20 kv. For calculation of structural formulae, analyses were normalized to the total number of oxygens in the mica. Analytical conditions and calibration used for EPMA analysis of mica are detailed in ESM2A.

Concentrations of Si, Li, Zn, Rb, Sr, Nb, Sn, Cs, Ba, Ta and W in white-mica were determined on thin sections by LA-ICP-MS. These analyses were performed at the Laboratoire Géoscience Océan of Brest using a Thermo Element 2 ICP-MS coupled with a Geolas 193-nm Excimer laser ablation system. Ablations were performed with a fluence of 6  $\text{J}/\text{cm}^2$ , a laser shot frequency of 10 Hz and beam size of 50 and 75  $\mu\text{m}$ .

The content of Li, Be, B, Na, Al, Si, S, Ti, Ge, As, Rb, Sr, Nb, Sn, Sb, Ta and W in quartz were determined at BRGM (French Geological Survey) using a ThermoScientific X series II quadrupole ICP-MS coupled with a Cetac Excite 193 nm laser ablation system. Ablations were performed on thick sections with a repetition rate of 8 Hz and laser energy of 10  $\text{J}/\text{cm}^2$  with a beam size of 85  $\mu\text{m}$ . For both quartz and white-mica analyses, ablated material was transported from the laser ablation cell by a He gas with a flow rate of 250 mL/min. Analyses comprise 20 s of gas blank measurement following by 60 s of ablation. Detailed analytical conditions and calibration used for trace elements analysis of white-mica and quartz are provided respectively in ESM2B and ESM2C.

Data reduction was performed with Glitter 4.0 (<http://www.glittergemoc.com/>) using the NIST SRM-612 glass standard for external standardization (Pearce *et al.*, 1997) and  $\text{Si}^{29}$  as internal standard for both quartz and mica.

#### 3.4 Principal component analysis

To investigate signature of white-mica and quartz composing the magmatic-hydrothermal system of Panasqueira, principal component analysis (PCA) was performed on the different populations of white-mica and quartz, which were distinguished based on their geological (magmatic, hydrothermal related to greisenization and hydrothermal related to mineralized veins) and petrographic characteristics. Principal component analysis (PCA) is a multivariate statistical method that permits to reduce large dataset into only two variables for plotting and clustering purposes and identify correlations between variables (Anderson, 2001). This approach uses an orthogonal transformation to convert variables into a set of principal components (PC), which correspond to linear combinations of the initial variables. The first principal component (PC1) retains the maximum variance present in the original dataset. In geosciences, this method is powerful tool to constrain the compositional variations of minerals between different populations and to investigate the behaviour of elements during geological processes (Winderbaum *et al.*, 2012; Belissant *et al.*, 2014; Codeço *et al.*, 2020). In order to avoid of left-censored data, elements characterized by concentrations close or below to the detection limit (bdl) were not included in the PCA.

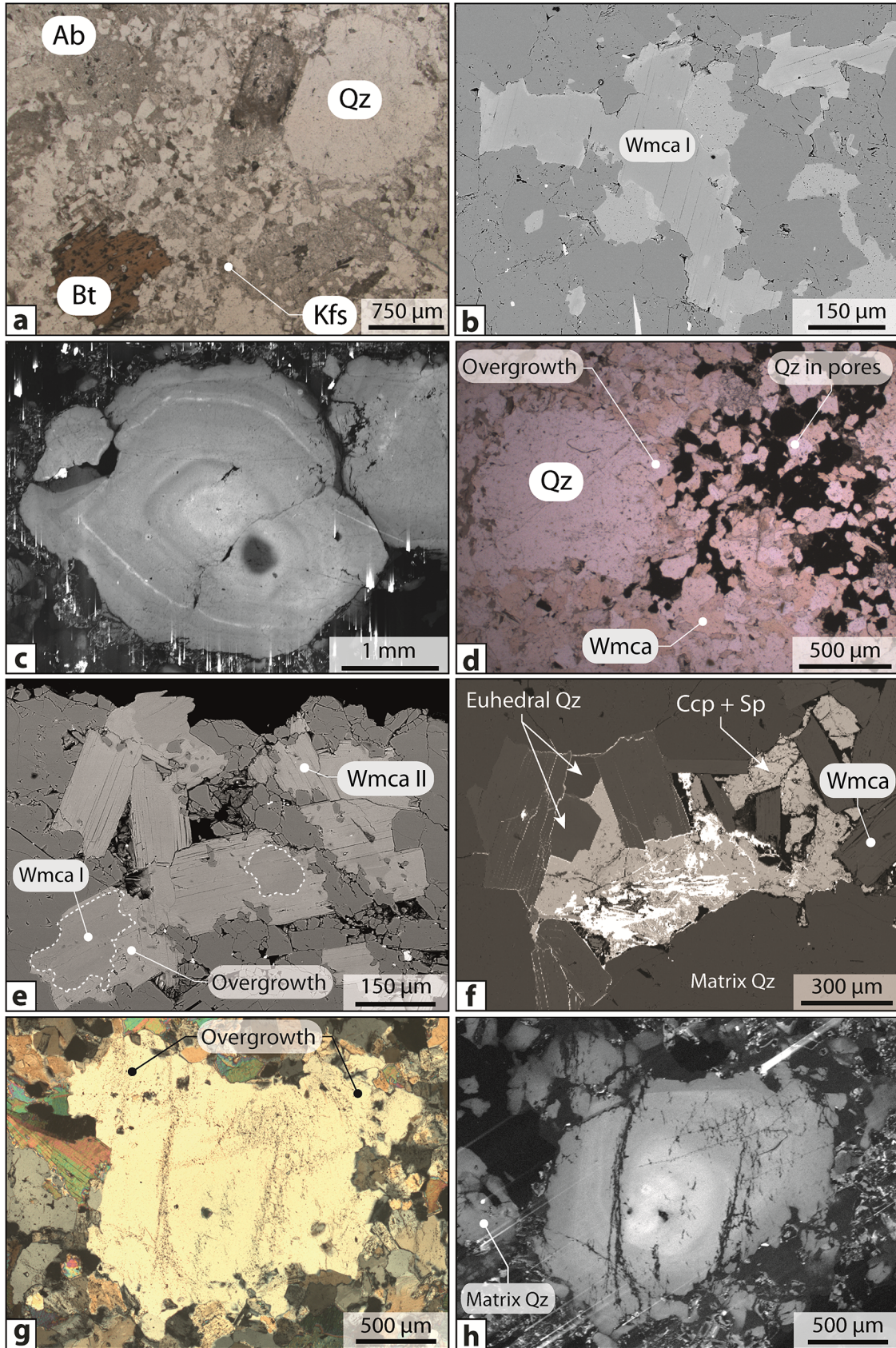


**Fig. 3.** Photomicrographs, SEM-BSE and SEM-CL images showing the textural characteristics of white-mica and quartz composing the two-mica granite and greisen of Panasqueira. (a) General view displaying the mineralogical composition and the texture of the two-mica granite. (b) SEM-BSE image of large flakes of magmatic white-mica displaying unzoned microtexture. (c) SEM-CL image of euhedral magmatic quartz phenocryst composing the two-mica granite of Panasqueira. This quartz exhibits a relatively weakly contrasted concentric growth zoning. (d) General view displaying the mineralogical composition and the texture of greisen. Note that vugs developed during greisenization were infilled by euhedral hydrothermal quartz and late sulfides and carbonate assemblages. (e) SEM-BSE image of white-mica composing the greisen of Panasqueira. These white-micas exhibit a strong zoning corresponding to hydrothermal overgrowth of primary magmatic white-mica of the two-mica granite. (f) SEM-BSE image of euhedral hydrothermal quartz infilling vug of greisen. Transmitted light (f) and SEM-CL (g) images of remnants of primary magmatic euhedral quartz phenocryst partially altered during greisenisation. These quartz exhibit hydrothermal overgrowths characterized by lower luminescence intensity than primary euhedral quartz phenocrysts cores. In some cases the primary concentric growth zoning are conserved. The CL-dark structures correspond to healed fractures underlined by fluid inclusions trails in transmitted light. Ab: Albite; Bt: Biotite; Kfs: K-feldspar; Wmca: White-mica; Qz: Quartz.

### 3.5 U–Pb dating of apatite

U–Pb dating of apatite (magmatic and hydrothermal) was conducted by in-situ LA-ICP-MS analyses at the GeoOHeLiS analytical platform (Geosciences Rennes/OSUR, Univ. Rennes) using a quadrupole Agilent 7700x ICP-MS coupled to ESI NWR193UC excimer laser. Apatite was ablated with a constant spot diameter of 50  $\mu\text{m}$  for an ablation rate of 5 Hz. The ablated material was then carried to ICP-MS by He mixed with  $\text{N}_2$  and Ar. Analyses were performed according to the analytical procedure described by Pochon *et al.* (2016) and detailed in ESM2D. Analyses of apatite were bracketed by analyses of different apatite standards comprising (i) the Madagascar apatite standard (ID-TIMS age of  $473.5 \pm 0.7$  Ma; Cochran *et al.*, 2014) used as the primary apatite reference and (ii) the Durango ( $31.4 \pm 0.12$  Ma; McDowell *et al.*, 2005) and the McClure ( $523.5 \pm 2.1$  Ma; Schoene and Bowring, 2006) apatite standards used to control the reproducibility and accuracy of measurements. Data reduction was carried out with the Iolite software (Paton *et al.*, 2010) and the data reduction scheme VizualAge UcomPbine (Chew *et al.*, 2014). Concordia diagrams and age calculations were done using ISOPLOT (Ludwig, 2012). All ages are quoted at 2 sigma.

## 4 Microtextures of quartz-white mica assemblages

### 4.1 Two-mica granite

The mineralogical and the textural characteristics of the two-mica granite of Panasqueira are displayed in Figure 3a (more photos are available in ESM3A). As described previously, this granite exhibits a porphyritic, coarse-grained texture (Fig. 3a). White-mica forms individual large sub-euhedral flakes (up to 1–2 mm) (Fig. 3b) consistent with a primary magmatic origin according to textural criteria (Miller *et al.*, 1981). They occur as interstitial grains in the rock matrix and as micaceous aggregates. Although most of the white-mica crystals appear to be igneous in origin, some little flakes can be observed along grain boundaries of biotite and feldspars and could represent the product of a hydrothermal alteration of these minerals. Backscattered electron images show that white-mica is characterized by a homogeneous chemical composition (Fig. 3b).

Quartz occurs as large euhedral phenocrysts (up to 0.5 cm) characterized by straight and sharp boundaries (Figs. 3a and 3c). The presence of fluid inclusions trails attests that quartz phenocrysts were affected by fracturing and healing mecha-

nism that occurred after the granite cooling (Fig. 3c). As evidenced by cathodoluminescence images (CL), these quartz phenocrysts exhibit weakly contrasted, oscillatory growth zoning (Fig. 3c). Cores are generally marked by a higher luminescence intensity than the rims. Fluid inclusions trails observed in transmitted light correspond to CL-dark structures defining healed vein-like structures that result from the precipitation of non-luminescent quartz within fractures planes (Rusk and Reed, 2002). Quartz occurs also as small xenomorph grains in the granite matrix (Fig. 3a). This second population of quartz is usually characterized by low CL and displays the same luminescence intensity than the rims of the euhedral quartz phenocrysts.

### 4.2 Greisen

Mineralogical and textural characteristics of the quartz-white mica assemblage from greisen are displayed in Figure 3d (more photos are available in ESM3B). Petrographic observations show that greisenization of the two-mica granite has caused the total breakdown of biotite and feldspars, which were wholly replaced by white-mica and quartz. During this intense metasomatic alteration the primary magmatic texture was completely obliterated. However, relics of euhedral quartz phenocrysts and primary magmatic white-mica can still be observed in greisen (Fig. 3d).

White-mica composing the massive greisen forms large sub-euhedral flakes (Figs. 3e and 3f). Some of them are characterized by a well-developed growth zoning marked by dark cores and light rims in SEM-BSE images (Fig. 3e). The contact between core and rim is well defined and the thickness of rims ranges between 50 and 300  $\mu\text{m}$ . Such pattern was already described in ongonites (Dostal *et al.*, 2015) and in the hydrothermally altered Sn-bearing granite of Ervedosa (northern Portugal) (Gomes and Neiva, 2000). This zoning pattern is usually interpreted as a marker of the hydrothermal alteration related to a mineralization event. Accordingly, these zoning can be interpreted as hydrothermal overgrowths on the primary magmatic white-mica during greisenization. Hydrothermal white-mica that have exclusively crystallized during greisenization (WmcaII) exhibit a homogeneous light color and are generally unzoned (Fig. 3e).

Remnants of primary magmatic quartz phenocrysts that were partially altered during greisenization can be observed in the greisen (Figs. 3d and 3g). They are generally characterized by irregular shape marked by the presence of hydrothermal overgrowths likely formed during greisenization (Figs. 3g and 3h).

Inclusions of albite and white-mica can be observed in these hydrothermal overgrowths (Fig. 3g). In cathodoluminescence images, these grains exhibit irregularly shape CL-light cores (primary magmatic quartz phenocrysts) surrounded by very weak luminescent quartz (hydrothermal overgrowth) (Fig. 3h). Quartz composing the greisen matrix and formed during greisenization by feldspars and biotite replacement is xenomorph and characterized by a low luminescence intensity (Fig. 3h). The euhedral quartz observed in the greisen porosity in association with cassiterite and sulfides (Figs. 3d and 3f) is marked by very weak CL equivalent to those observed in the matrix quartz. Secondary features under the form of healed fractures are common in all quartz composing the massive greisen.

### 4.3 Ore-bearing quartz veins

The textural characteristics of the white-mica-rich selvage along schist-vein contacts and quartz related to the QTS and MOSS are displayed in Figure 4 (more photos are available in ESM3C). White-mica selvages exhibit a fibrous texture composed of large euhedral flakes (that can reach 3 cm of height) that grew vertically during the opening of veins (Fig. 4a). White-mica is generally found in direct continuity with tourmaline formed during the quartz tourmaline stage (QTS) and can be associated with apatite, cassiterite and wolframite (Fig. 4a). This white-mica is generally unzoned but brighter-luminescent overgrowth can be locally observed.

In the hydrothermal veins, quartz crystals appear as prismatic phenocrysts that can reach ~20 cm in length. In general, quartz grew vertically and perpendicular to the vein edge. On sections perpendicular to their axis, quartz exhibit typical euhedral shape surrounded by large open space, in which cassiterite and wolframite have crystallized (Figs. 4b and 4c). Tourmaline is generally prior and included within these crystals of quartz (Fig. 4b). As evidenced by CL images this quartz is characterized by thin, contrasted, oscillatory growth zoning (Figs. 4d and 4e). Corrosion textures can be observed and emphasize that quartz could be partially dissolved and re-crystallized (Fig. 4e). Hydrothermal quartz is also characterized by the presence of a dense network of secondary features such as fractures filled by non-luminescent quartz (Figs. 4d and 4e).

## 5 Whole-rock geochemistry

Bulk analyses of the two-mica granite, greisenized granite and greisen of Panasqueira are provided in ESM4. Results of PCA performed on all whole-rock elemental compositions are displayed in Figure 5a. A set of 21 variables including major (Fe, Mg, Ti, Ca, Al, Na, K, Mn and P) and the main trace elements (Li, Ba, Cs, Nb, Ta, Rb, Sr, W, Sn, Zn, Cu and  $\Sigma$ REE) has been selected for this PCA. The PC1 vs. PC2 projection plane (Fig. 5a) accounts for 66.3% of the total variance of the dataset, with 50.4% for PC1 and 15.9% for PC2. Samples of two-mica granite (black dots on the left side in Fig. 5a) are separated of greisen samples (white dots on the right side in Fig. 5a) by PC1, which is strongly influenced by metal-granophile elements (Cs, Sn, W, Li, Cu and Zn). The greisenized granite samples (grey dots) occupy an intermediate

position between the granite and greisen endmembers. Five groups in which elemental concentrations are positively correlated can be distinguished (Fig. 5a): group 1 (Mg, Ti, Ba and Ca), group 2 (Na, Sr and  $\Sigma$ REE), group 3 (Mn and K), group 4 (Fe, Rb, P, Sn, W, Li, Cs, Cu, Zn and Al) and group 5 (Nb and Ta). Elements composing groups 4 and 5 are anti-correlated with elements composing groups 1 and 2 (Fig. 5a). Granite is generally rich in elements from groups 1 and 2 whereas greisen is enriched in elements from groups 4 and 5.

In order to constrain mass changes (i.e element gains and losses) and element mobility related to greisenization, a mass balance calculation was performed using the Grant's (Grant, 1986) isocon approach (Fig. 5b). The best fit isocon (blue line in Fig. 5b) is drawn using Al, Mn and P, assuming that these elements were conservative and relatively immobile during greisenization. The slope of this isocon (~1.18) suggests an important mass loss during greisenization that is consistent with the abundant porosity observed in greisen (Launay, 2019). Individual element mass changes calculated from the isocon are displayed in diagram of relative mass changes (Fig. 5c). Greisen is marked by an overall enrichment in Fe (24%), K (20.5%), Cs (72%), Rb (77%), Li (70%), Sn (170%), W (129%), Nb (58%), Ta (69%), Cu (7000%) and Zn (1120%) and depletion in Si (-18%), Mg (-32%), Ca (-35%), Na (-95%), Ti (-44%), Ba (-39%), Sr (-49%), Zr (-61%) and REE (-87%). This evolution is consistent with element clusters identified by PCA and reflect the mineralogical control on the incorporation and releasing of elements during fluid-rock interactions related to greisenization.

## 6 White-mica geochemistry

Major and trace elements compositions of white-mica composing the two-mica granite, greisenized granite, the massive greisen and the mineralized veins of Panasqueira are provided in ESM5 and ESM6.

### 6.1 General features and classification

All white-mica described previously are classified according to the discriminating diagrams of Miller *et al.* (1981) and Monier and Robert (1986) (Figs. 6a and 6b). White-mica composing the two-mica granite falls in the primary muscovite field (Fig. 6a) and is characterized by compositions close to theoretical muscovite from the classification of Monier and Robert (1986) (Fig. 6b). Hydrothermal white-mica from the greisen plot in the secondary muscovite field (Fig. 6a) and are characterized by compositions ranging from muscovite to Zinnwaldite (Fig. 6b). In chemical maps (Fig. 6c), the zoning observed in some white-mica from greisen corresponds to core to rim depletion in Al and Ti and core to rim enrichment in Fe and Mg. Cores plot in the primary muscovite field, while rims plot in the secondary muscovite field and exhibit compositions similar to hydrothermal muscovite that formed during greisenization (Figs. 6a and 6b). Accordingly, rims correspond likely to hydrothermal overgrowth of primary magmatic muscovite that crystallized during greisenization. Hydrothermal white-mica forming selvages along schist-vein contacts are characterized by compositions ranging from trillithionite to zinnwaldite (Fig. 6b) and plot in part in the secondary muscovite field (Fig. 6a).

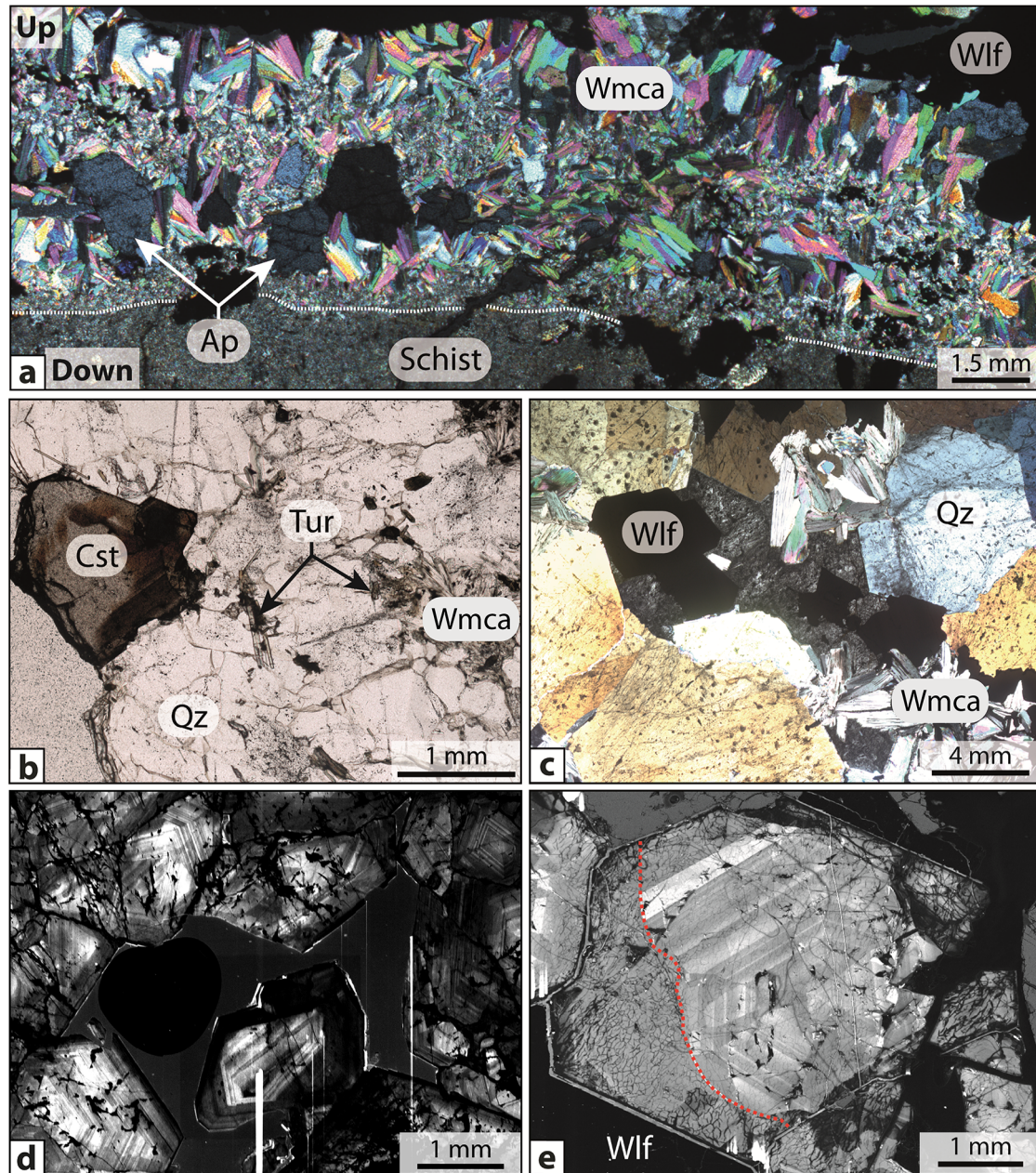


**Fig. 4.** Photomicrographs and SEM-CL images showing the textural characteristics of white-mica and quartz related to the QTS and MOSS of the mineralized veins of Panasqueira. (a) Vertical section perpendicular to the horizontal vein planes showing a white-mica-rich selvage associated with early apatite and overlain by wolframite. (b) and (c) transmitted light images of hydrothermal quartz respectively formed during to the QTS and the MOSS. These sections were cut horizontally and perpendicular to the axis of quartz. (d) and (e) SEM-CL images displaying textural characteristics of quartz formed during the QTS and the MOSS. These hydrothermal quartz exhibit thin, contrasted, oscillatory growth zoning. The dense network of CL-dark structures corresponds to fractures healed by non-luminescent quartz. Quartz can be partially corroded (red dashed line in e) and marked by sector zoning. Ap: Apatite; Cst: Cassiterite; Wmca: White-mica; Qz: Quartz; Tur: Tourmaline; Wlf: Wolframite.

## 6.2 Major and trace elements compositional characteristics

Results of PCA performed on white-mica compositions are displayed in Figure 7a. PC1 and PC2 account respectively for 42.6% and 21.9% of the total variance of the dataset. The clustering of elements as well as the different populations of

white-mica can be observed on the PC1 vs. PC2 projection plane (Fig. 7a). PC1 clearly separates magmatic muscovite (Wmca I) from the two-mica granite and the muscovite cores from the greisenized facies and the hydrothermal white-micas found in the greisen (Wmca II) and the vein selvages. PC1 is mainly influenced by Rb, Cs, Zn and to a lesser extent by F, Sn, W, Mg, Li and Ba. Five element correlation clusters can be

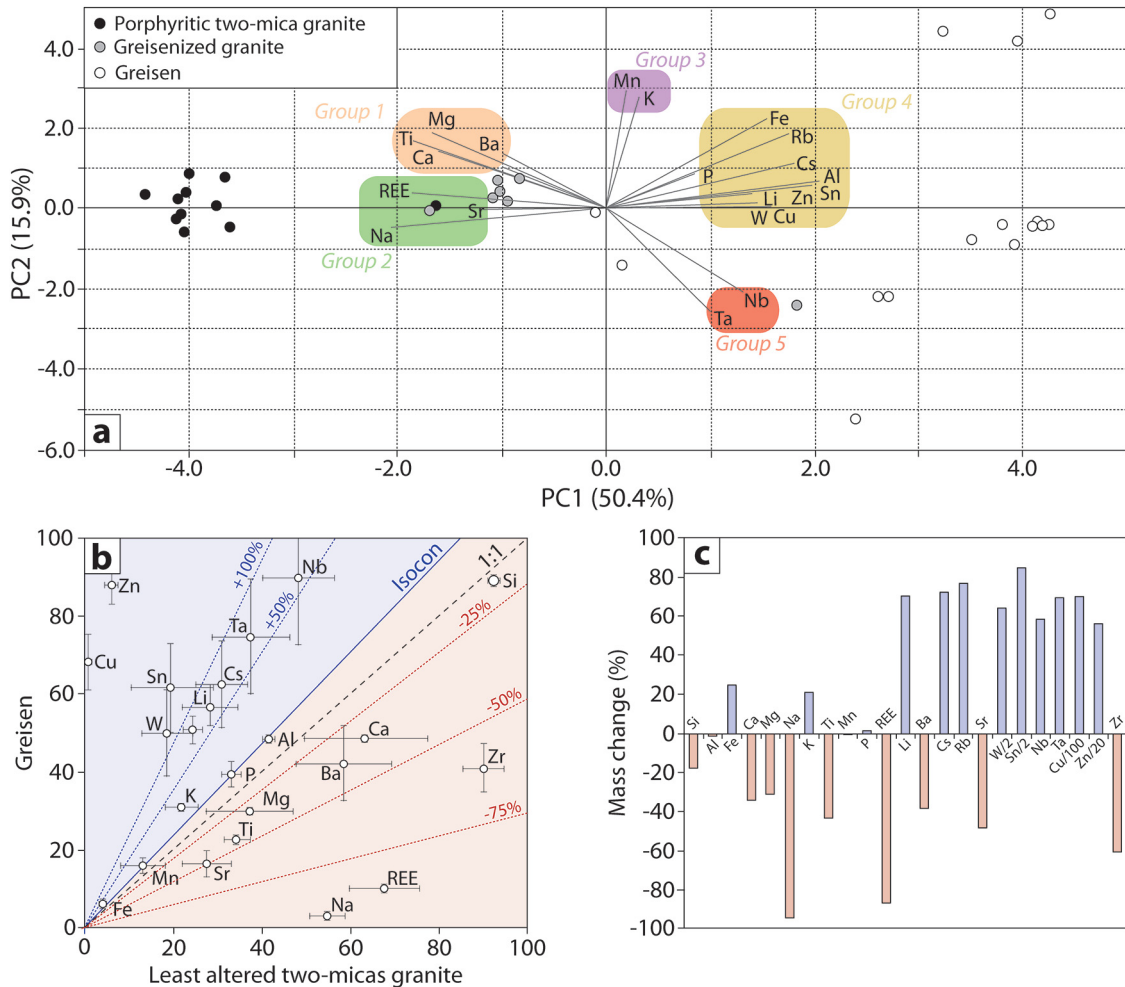


**Fig. 5.** (a) Biplot PC1 vs. PC2 diagram displaying results of principal components analysis (PCA) performed on major and trace element compositions of granite, greisenized granite and greisen. (b) Isocon diagram displaying the mobility of elements during greisenization. The lines with percentage values correspond to the net percent gains and losses relative to the isocon (blue line). Granite and greisen compositions are respectively an average of the 11 least altered granite and the 3 most altered samples of greisen. (c) Major and trace elements mass changes in greisen relative to the best-fit isocon.

distinguished (Fig. 7a): group 1 (Si and Sr), group 2 (Na and Al), group 3 (Ba, Mg, Sn, W, Li and F), group 4 (Rb, Cs and Zn) and group 5 (Fe, Nb and Ta). Elements composing group 4 are positively correlated with elements composing groups 3 and 5 and anti-correlated with elements composing group 2 (Fig. 7a). Elements composing groups 3 and 4 are strongly anti-correlated with Ti.

As highlighted from binary diagrams (Figs. 7b–7g) and the PC1-PC2 projection plane, primary magmatic muscovite (Wmca I) is richer in Al, Ti and Na and poorer in Fe, Mg, F, Cs, Rb, Li, Zn, Sn and W than secondary hydrothermal white-mica forming the greisen (Wmca II) (rims of zoned white-mica and white-mica formed by replacement of feldspars). Figure 7b shows that the lower Al content in hydrothermal white-mica from the greisen is balanced by addition of Fe and Mg in the octahedral site by the substitution vector  $(\text{Mg}, \text{Fe})^{\text{VI}} \leftrightarrow \text{Al}$  explaining the higher Fe and Mg concentrations in white-mica composing greisen. The increase of Rb content between magmatic and hydrothermal white-mica of greisen is accompanied

by significant increase in Cs, Li and Zn concentrations (Figs. 7d–7f). The Sn and W variations during greisenization are positively correlated and increase respectively from 60 to 414 ppm and 10 to 43 ppm (Fig. 7g). Hydrothermal white-mica from ore-bearing quartz veins have intermediate compositions in Al, Mg, Fe and F between magmatic and hydrothermal white-mica from greisen (Figs. 7b and 7c). They are also characterized by similar compositional ranges in Li, Ba, Cs, Rb and Zn and higher concentrations in W (between 65 and 156 ppm) and Sn (between 229 and 879 ppm) than hydrothermal white-mica composing greisen.

## 7 Quartz chemistry

### 7.1 Chemical characteristics of the different populations of quartz

Trace elements contents for the different populations of quartz are reported in spider diagrams (Fig. 8). The entire

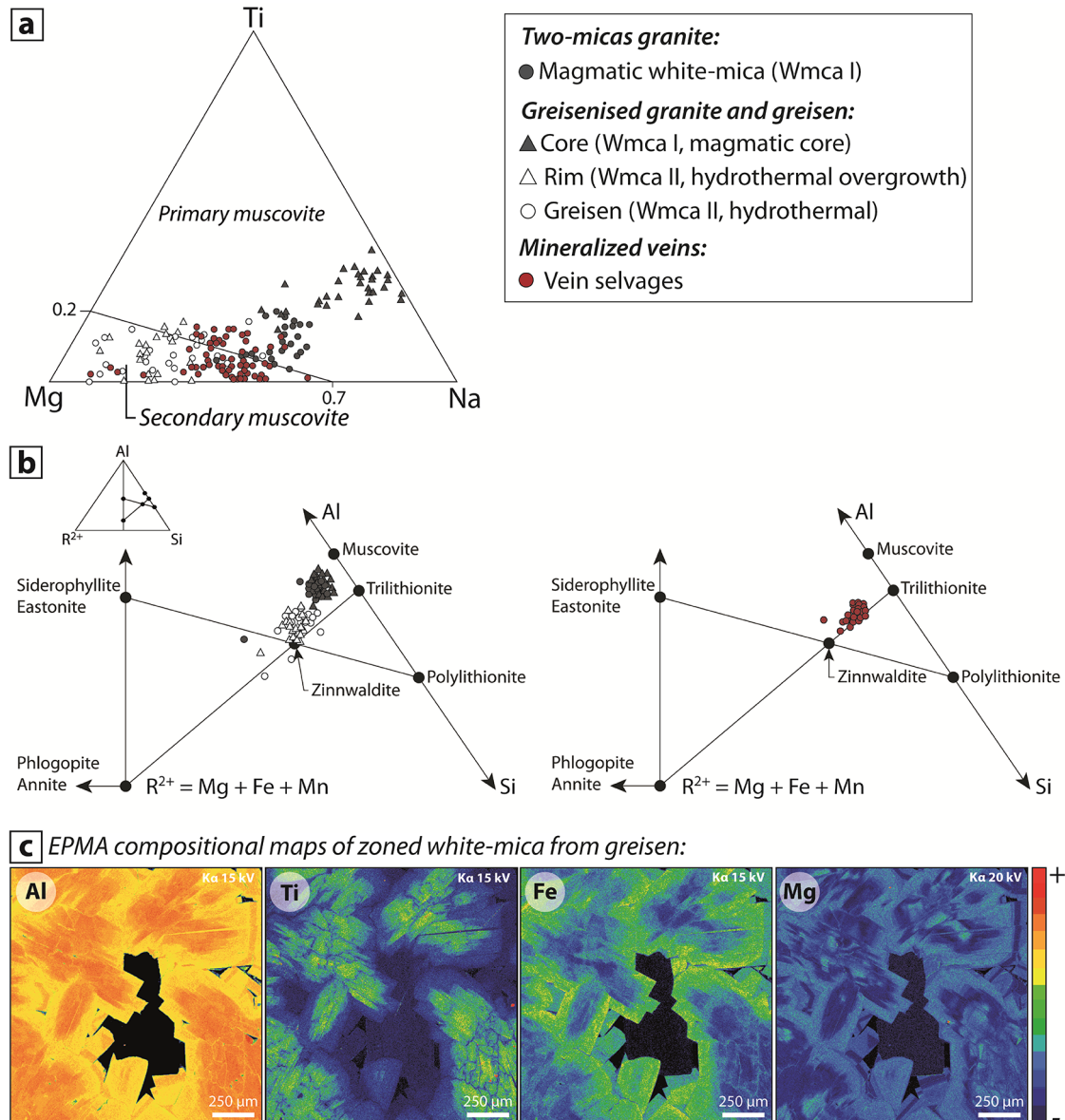


**Fig. 6.** Geochemical characteristics of white-mica composing the two-mica granite, greisenized facies, the massive greisen and the mineralized veins selvages of Panasqueira. (a) Ternary Ti–Na–Mg diagram displaying the fields of primary and secondary muscovite (after Miller *et al.*, 1981). (b) Compositions of white-mica plotted in the mineralochemical phase diagrams (Al–(Fe + Mg + Mn)–Si) of Monier and Robert (1986). (c) Chemical maps of Al, Ti, Fe and Mg of white-mica composing the greisen of Panasqueira. These white-micas exhibit a strong chemical zoning corresponding to hydrothermal overgrowths of primary magmatic muscovites.

dataset is available in [ESM7](#). Although most of the elements were detected in all the analyzed quartz crystals, concentrations of Be, Nb, Ta, Sn and W were often close to their detection limits (0.05 ppm for Be and 0.01 ppm for the other). Al, Li, Ti, Na and S are the most abundant elements (several tens to several hundreds of ppm) in all quartz populations. Light elements like Ge and B are also quite enriched (up to several tens of ppm), whereas heavy element contents (from As to W) are generally lower and characterized by wide ranges of concentrations (Fig. 8). Nb and Ta were generally not detected and therefore not considered to discriminate the

different quartz populations. Al, Ti and Rb depict peaks specific of magmatic quartz, while the Ge, B, As and W contents are generally higher in the hydrothermal quartz found in both the greisen and mineralized veins (Fig. 8).

*Quartz from the unaltered two-mica granite:* Cores of magmatic euhedral quartz phenocrysts are characterized by high contents in Ti (> 136 ppm), Al (> 295 ppm) and Li (> 10 ppm) and low content in B (< 3.4 ppm) and Ge (< 0.9 ppm) (Fig. 8a). Quartz phenocrysts are generally marked by slight core to rim enrichments in Ge (from 0.6 to 1.1 ppm), B (from 2.1 to 4.2 ppm) and Na (from 14 to 22 ppm)

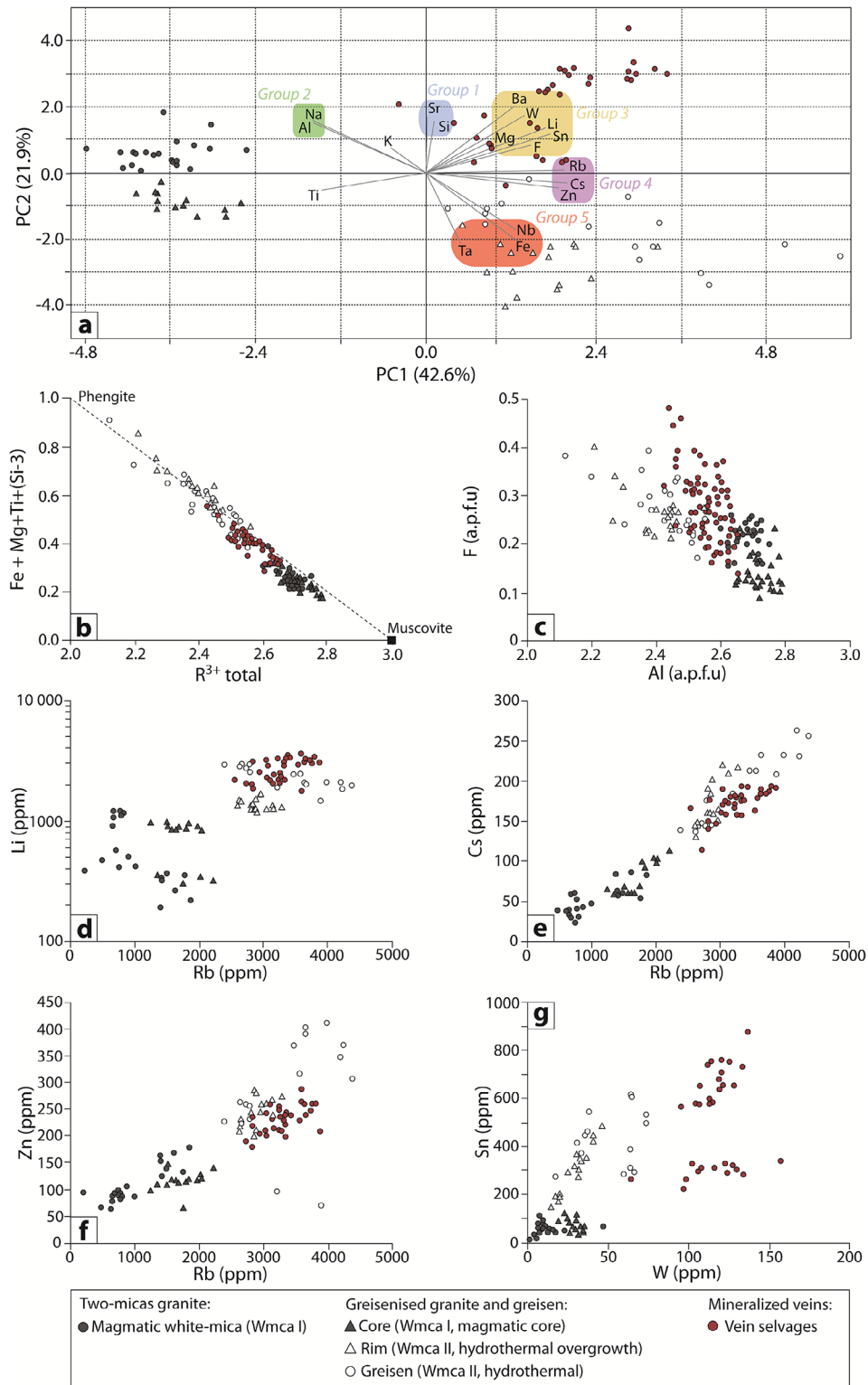


**Fig. 7.** (a) Biplot PC1 vs. PC2 diagram displaying results of principal components analysis (PCA) performed on major and trace element compositions of the different generations of micas composing the two-mica granite, the greisenized facies, the greisen and the mineralized vein selvages of Panasqueira. (b) Diagram illustrating ideal dioctahedral substitutions for different populations of micas (after Guidotti, 1984). (c) to (g) Binary diagrams displaying the major and trace element content for the different generations of white-mica considered in this study. The elements pairs displayed in these diagrams were defined from PCA performed on the white-mica composition dataset.

and by slight core to rim depletion in Ti (from 183 to 64 ppm), Li (from 23 to 13 ppm), Al (from 408 to 263 ppm) and Rb (from 2.2 to 1 ppm; values refer to median values for cores and rims) (Fig. 8a). These rims also exhibit highly variable concentrations in Be, As, Rb, Sr, Nb, Sn, Sb and W. Quartz from the granite matrix are characterized by the same median concentrations in trace elements than the rims of quartz phenocrysts (Fig. 8a).

*Quartz from the massive greisen:* Cores of euhedral quartz phenocrysts preserved in greisen exhibits the same spider diagram pattern and is characterized by the same compositional ranges as quartz phenocrysts of the unaltered two-mica granite (Fig. 8b). It displays the same typical peaks in Ti, Al and Rb previously described in magmatic quartz with almost the same median values of concentrations. This suggests that despite the strong fluid-rock interactions related to greisenization, the primary magmatic signature of quartz phenocrysts was conserved in greisen. Hydrothermal overgrowth of these quartz phenocrysts are characterized by a spider diagram pattern significantly different than magmatic quartz phenocrysts, with lower content in Ti (< 36 ppm), Al (< 140 ppm) and Rb (< 1.2 ppm) and higher content in Ge (> 1.8 ppm), B (> 3.1 ppm) and Na (> 20 ppm) (Fig. 8c). Euhedral quartz from the greisen porosity exhibits the same signature than (i) quartz composing the greisen matrix and (ii) hydrothermal overgrowth of quartz phenocrysts (Fig. 8b). These different generations of quartz are marked by (i) the absence of peaks in Ti and Rb, (ii) highly variable concentrations in As, Rb, Sr, Nb, Sn, Sb and W and (iii) higher contents in B, Na and Ge compared to magmatic quartz.

*Quartz from the mineralized veins:* Hydrothermal quartz from the wolframite-bearing veins related to the quartz-tourmaline (QTS) and the W–Sn mineralization stages exhibits signatures clearly different from those of magmatic quartz but similar to the signatures of hydrothermal quartz from the greisen. This is characterized by (i) absence of Ti and Rb peaks, (ii) lower contents in Al, Ti and Li and (iii) higher contents in Ge, B and Na than magmatic quartz (Fig. 8c). However, median As and B concentrations in hydrothermal quartz from veins are significantly higher than those of hydrothermal quartz from greisen. Although quartz formed during the W–Sn mineralization stage has similar chemistry to quartz formed during the QTS, it is characterized by lower median concentrations in B, Al and Ti and higher median concentrations in Na than quartz of the QTS (Fig. 8c).

## 7.2 Chemical evolution trends

Results of PCA performed on the trace element compositions of quartz are shown in Figure 9a. The clustering of quartz populations is clear on PC1-PC2 projection plane. Magmatic quartz occurs on the right side of the diagram and is clearly separated of hydrothermal quartz that occurs on the left side (Fig. 9a). Higher concentrations in Ge, B, As and S (group 1) and lower concentrations in Li, Al, Ti and Rb (groups 2 and 3) distinguish hydrothermal quartz (from greisen and mineralized veins) from magmatic quartz. As expected from PCA, Li and Al (group 2) show positive linear correlation (Fig. 9b) for both magmatic quartz and the different generations of hydrothermal quartz. This correlation commonly described

in magmatic-hydrothermal systems (Breiter *et al.*, 2017a, 2017b; Müller *et al.*, 2018; Monnier *et al.*, 2018) is due to the coupled substitution  $\text{Al}^{3+}-\text{Li}^+ \leftrightarrow \text{Si}^{4+}$  (Weil, 1984; Heaney *et al.*, 1994; Götzte *et al.*, 2004). The chemical trend depicted in the Li vs. Al diagram exhibit a progressive depletion in Al and Li from magmatic quartz of the two-mica granite to hydrothermal quartz of greisen and mineralized veins (Fig. 9b). The Ge and Ti have a negative correlation (Figs. 9a and 9c) with a progressive Ti depletion and Ge enrichment from magmatic to hydrothermal quartz of greisen and mineralized veins. This negative correlation is typical in magmatic-hydrothermal system worldwide and is commonly used as indicator of magmatic-hydrothermal evolution (Müller *et al.*, 2002; Jacamon and Larsen, 2009; Breiter *et al.*, 2012, 2017a, 2017b). The Ge/Ti ratio provides a reliable index to track the magmatic-hydrothermal transition in the mineralized system of Panasqueira. The Al, Li, Rb and B vs Ge/Ti diagrams (Figs. 9d–9g) show that the magmatic-hydrothermal evolution of Panasqueira defined by an increase of Ge/Ti ratio in quartz is marked by a progressive depletion in Al, Li and Rb and by a progressive enrichment in B from magmatic to hydrothermal quartz (greisen and veins). In these different trends, greisen quartz has a intermediate compositions which overlaps both compositions of magmatic quartz from the two-mica granite and hydrothermal quartz from veins. This overlap is probably caused by the occurrences of relic magmatic quartz phenocrysts in the greisen and the crystallization of quartz equilibrated with hydrothermal mineralizing fluids during greisenization.

## 8 U–Pb dating of apatite

In the cathodoluminescence images, the primary magmatic apatite commonly displays homogeneous dark-grey luminescence (Fig. 10a). However, some grains were slightly altered along the edges and exhibit a lighter-grey-luminescent rim (Fig. 10a). Thus, only the unaltered parts of the grains were considered for U–Pb dating.

During greisenization of the two-mica granite, the primary magmatic apatite was partially preserved. Cathodoluminescence imaging shows the progressive alteration and replacement of the primary magmatic apatite (Fig. 10b). When alteration is incomplete, the magmatic apatite is replaced by hydrothermal apatite along the grain edges and along microfractures. The magmatic apatite grains that were the most affected by hydrothermal alteration exhibit complex patchy-zoning textures consistent with a strong pervasive alteration related to greisenization (Fig. 10b). The occurrences of thin oscillatory zoning (hydrothermal overgrowth) that surrounded some altered grains which demonstrate that a second generation of hydrothermal apatite was formed (Fig. 10b). Unfortunately, the dating of this second generation of apatite was not possible due to their high content in non-radiogenic lead.

Several generations of apatite can be distinguished in the mineralized veins of Panasqueira. Here we focus on the first generation of apatite whose crystallization accompanied the formation of the muscovite selvage and marked the early stages of vein formation (MOSS). Cathodoluminescence images of these hydrothermal apatite crystals display oscillatory zoning corresponding to growth bands (Fig. 10c).

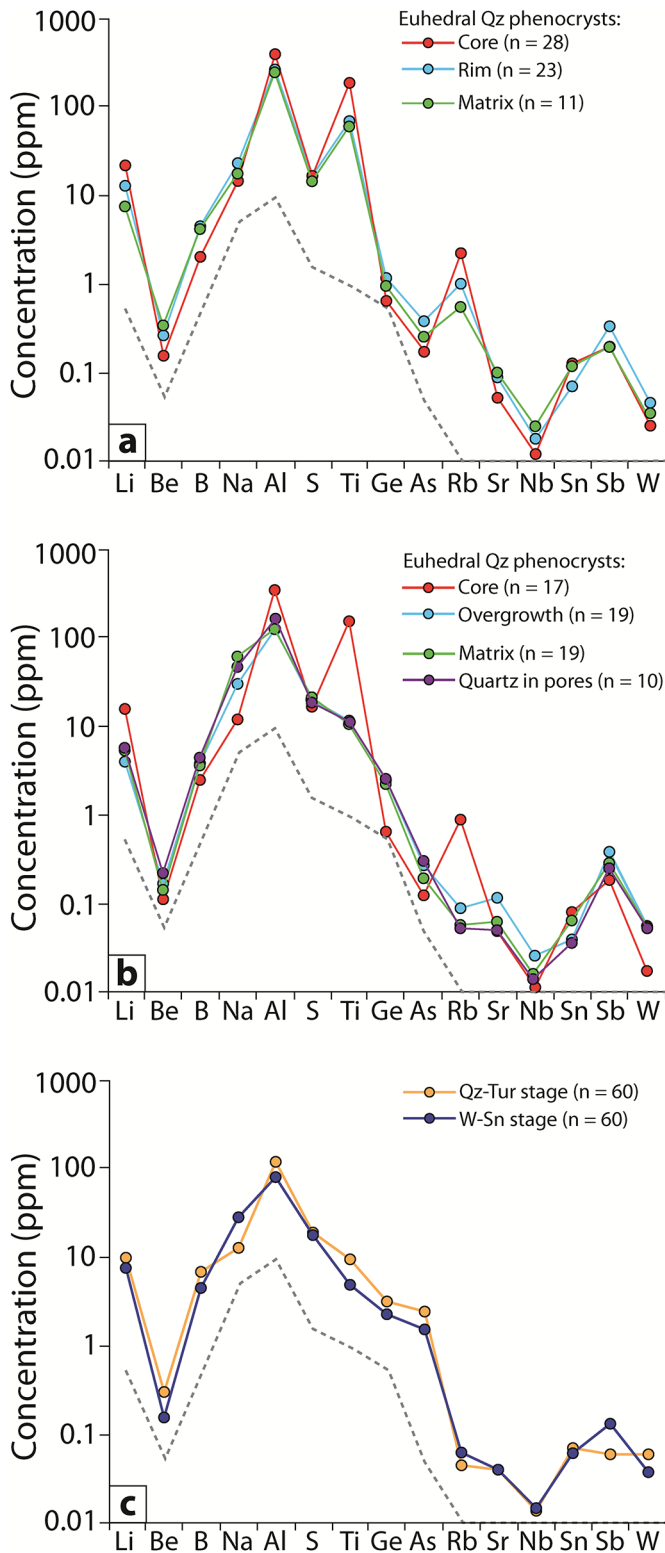


**Fig. 8.** Spider diagrams displaying the median values of trace element contents in the different generations of quartz considered in this study for (a) the two-mica granite, (b) the greisen and (c) the wolframite-bearing veins. The grey dashed line corresponds to the detection limit.

U–Pb analyses of magmatic apatite from the two-mica granite, altered magmatic apatite from the greisen and hydrothermal apatite from the mineralized veins are given in *ESM8* and are reported in Tera–Wasserburg diagrams (Figs. 10d–10f). The ages are provided with  $2\sigma$  errors. All ages presented in the following section were obtained from discordant data without imposing the composition of the initial common Pb (unforced Discordia). In all 3 case, there is a good agreement between the  $(^{207}\text{Pb}/^{206}\text{Pb})_0$  ratios found with the discordia and the value calculated with the [Stacey and Kramer \(1975\)](#) Pb evolution model for an age of ca. 295 Ma.

A total of 23 analyses were performed on a dozen grains of primary magmatic apatite. They plot along a well-defined discordia with  $(^{207}\text{Pb}/^{206}\text{Pb})_0$  ratios ranging from 0.262 to 0.839 and yielding a lower intercept date of  $296 \pm 4$  Ma (MSWD = 0.6,  $n = 23$ ) (Fig. 10d).

For altered magmatic apatite observed in the greisen, we performed 36 analyses on over 15 different grains. Analyses display higher proportion of common Pb compared to magmatic apatite with  $^{207}\text{Pb}/^{206}\text{Pb}$  ratios ranging from 0.533 to 0.839. The unforced discordia yields a lower intercept date of  $292 \pm 10$  Ma (MSWD = 1.7,  $n = 36$ ) (Fig. 10e). The hydrothermal overgrowths (oscillatory zoning) surrounding the altered apatite grains have a very high proportion of common Pb (red ellipses on Fig. 10e) compared to altered grains.

For the hydrothermal apatite from the vein selvages, we performed 22 analyses out of 12 grains. These analyses display  $(^{207}\text{Pb}/^{206}\text{Pb})_0$  ratios ranging from 0.353 to 0.650 and yield an intercept date of  $295 \pm 5$  Ma (MSWD = 2.2,  $n = 22$ ) (Fig. 10f).

## 9 Interpretation and discussion

### 9.1 Incorporation of trace elements in quartz and interpretation of chemical trends

The largest variations in trace element contents in quartz was observed for Al, Ti, Li, Rb, Ge and B. Incorporation of Ti in quartz is partly dependent on the temperature of crystallization ([Wark and Watson, 2006](#); [Thomas \*et al.\*, 2010](#); [Huang and Audétat, 2012](#)). The progressive decrease of the Ti contents observed from magmatic to hydrothermal quartz reflects the progressive cooling of the magmatic hydrothermal system of Panasqueira.

Germanium is compatible in quartz and its incorporation is primarily controlled by the amount of Ge present in melt/fluid. In magmatic system, the increase in Ge contents is a robust indicator of magma fractionation ([Larsen \*et al.\*, 2004](#); [Müller \*et al.\*, 2010](#); [Breiter \*et al.\*, 2017a, 2017b](#); [Monnier \*et al.\*, 2018](#)), as Ge is preferentially concentrated in residual melt and fluids. At Panasqueira, the enrichment in Ge in hydrothermal quartz from greisen and W–Sn-bearing quartz veins suggest that greisenization and the formation of mineralized veins result from the circulation of magmatic fluids, in which Ge was concentrated during the progressive crystallization of the granite.

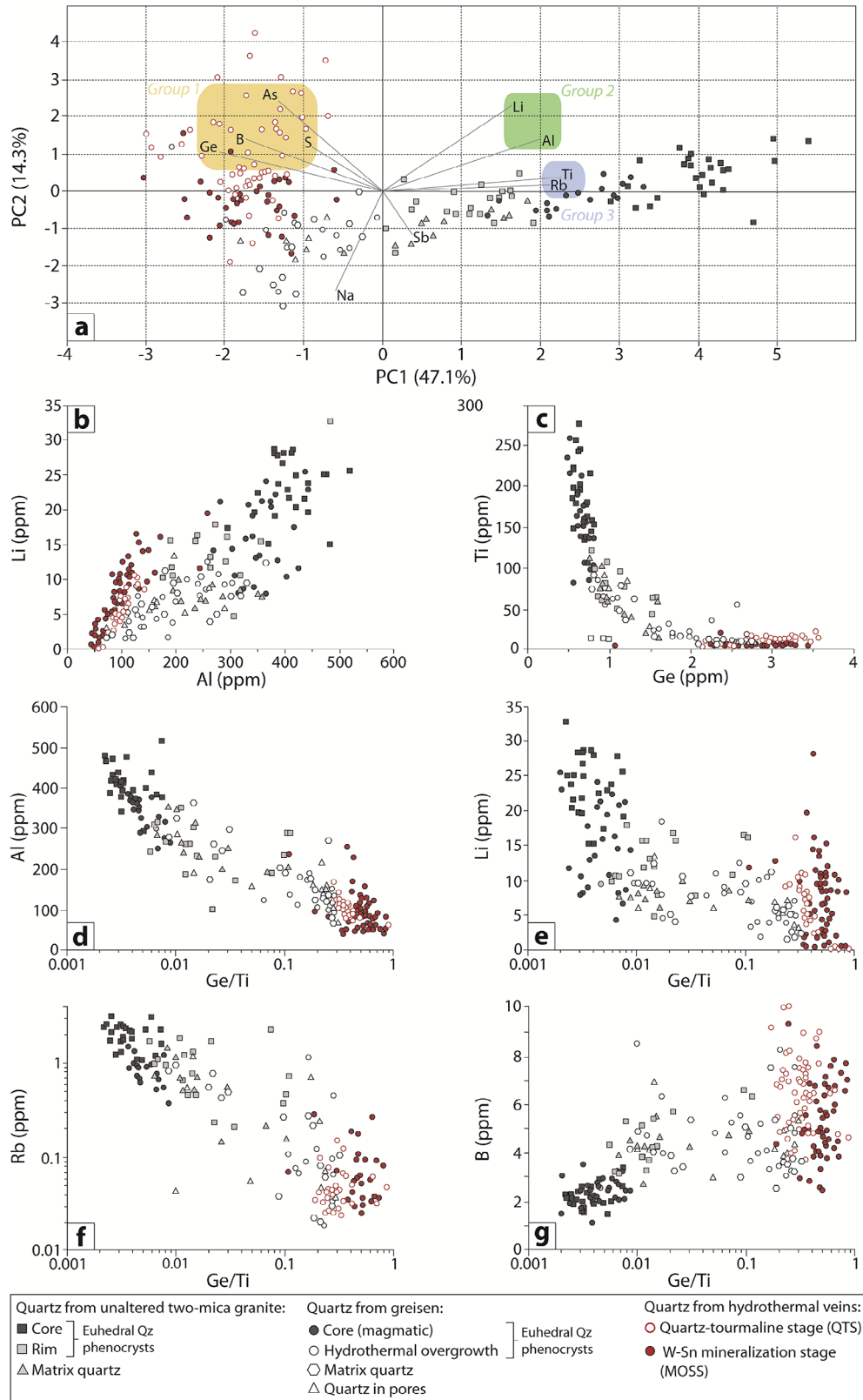


**Fig. 9.** (a) PC1 vs. PC2 projection plane displaying results of principal components analysis (PCA) performed on the main trace elements composing the different generations of quartz occurring in the two-mica granite, the greisen and the mineralized veins of Panasqueira. (b) to (g) Chemical evolution trends from magmatic to hydrothermal quartz displaying the behavior of Ti, Al, Ge, Li, Rb and B during magmatic-hydrothermal evolution of the Panasqueira ore deposit.

Li and Rb are generally considered as incompatible elements, which were preferentially concentrated in residual melt and magmatic fluids. Accordingly, hydrothermal quartz from greisen and mineralized veins should have higher concentrations of Li and Rb than magmatic quartz. However, compositional evolutions of quartz show the opposite trend with hydrothermal quartz having lower Li and Rb concentrations. This trend may be a result of (i) the crystallization of a large amount of white-mica both in greisen and within the mineralized veins that incorporate preferentially these elements and (ii) a limited incorporation of Al in hydrothermal quartz that consequently inhibits the incorporation of Li according to the coupled substitution  $\text{Li Al} \leftrightarrow \text{Si}$ . Although, the high Rb and Li contents in hydrothermal white-mica of greisen and veins support the first hypothesis, the low Al contents in hydrothermal quartz and the Li–Al correlation observed seem to confirm the second assumption.

The B enrichment observed from magmatic to hydrothermal quartz is consistent with the incompatible behavior of B that is preferentially concentrated in residual melt and tends to be expelled with magmatic fluids (Pichavant, 1981; London *et al.*, 1988). The circulation of these B-rich fluids resulting from crystallization of the Panasqueira granite explain the intense tourmalinization of metasedimentary host rock observed around the veins as well as the crystallization of quartz-tourmaline veinlets at the incipient stage of the hydrothermal activity (Codeço *et al.*, 2017; Launay *et al.*, 2018; Carocci *et al.*, 2018).

## 9.2 Chemical characteristics of fluids related to greisenization and veins

Composition of quartz-muscovite assemblages depends on temperature, pressure, composition of melt-fluids and crystal-melt or crystal-fluid partitioning coefficients. In the following, major and trace elements variations in quartz-white mica assemblages are used to monitor magmatic-hydrothermal processes and the geochemistry of hydrothermal fluids related to greisenization and the formation of mineralized veins. Compositions of quartz-white mica assemblages from greisen and mineralized veins demonstrate that fluids related to greisenization and the earliest stages of vein formation were rich in granophile elements (F, Li, Rb, Cs and B) and ore metals (W, Sn and Zn). These results are consistent with direct analysis of quartz-hosted fluid inclusions from mineralized veins performed by Lecumberri-Sanchez *et al.* (2017). They demonstrated that the fluids related to the W–Sn mineralization of Panasqueira are significantly enriched in (i) B, Li, Cs and Rb with concentrations up to several hundred of ppm and (ii) ore metals (W, Cu and Zn) with concentrations reaching several tens or hundreds of ppm. Herein, quartz-white mica assemblages from greisen and ore-bearing quartz veins have comparable chemical signatures. This implies a genetic link between greisenization and the formation of W–Sn-bearing quartz veins that resulted likely from the circulation of the same fluids.

## 9.3 Thermal evolution of the magmatic-hydrothermal system of Panasqueira from the TitaniQ thermometer

From experimental data and thermodynamic studies, several calibrations permitting to estimate temperature of

quartz crystallization from Ti concentration were proposed (Wark and Watson, 2006; Thomas *et al.*, 2010; Huang and Audétat, 2012). The relationship defined by Thomas *et al.* (2010) to estimate temperatures of crystallization for the different generations of quartz analyzed, is applied here. For this calculation, a pressure of 1 kbar is used according to values estimated by Bussink (1984) from fluid inclusions. Petrographic study provided evidence of occurrences of rutile in greisen and within mineralized veins associated to tourmaline (Carocci *et al.*, 2018). However, due to the difficulty to determine if these different populations of quartz and rutile are cogenetic, we consider values of  $a_{\text{TiO}_2}$  ranging from 0.2 to 1 for calculations (Fig. 11).

Calculations performed with Ti activity ( $a_{\text{TiO}_2}$ ) of 0.2 give relatively high crystallization temperatures for magmatic euhedral quartz phenocrysts (800 °C) that are inconsistent with crystallization temperatures of granitic melts. Conversely, calculations performed with Ti activity of 0.5 and 1 for magmatic quartz give temperatures ranging between 600 and 700 °C, which are more consistent with temperatures of granite crystallization (Tuttle and Bowen, 1958; Luth *et al.*, 1964; Ackerson *et al.*, 2018). Ranges of crystallization temperatures calculated for rims of quartz phenocrysts and for the matrix quartz of the two-mica granite are similar (500–600 °C) (Fig. 11). Accordingly, these two populations of quartz crystallized contemporaneously and later than cores of quartz phenocrysts. Hydrothermal quartz formed during the greisenization and the quartz-tourmaline stage (i.e the earliest stage of veins formation) exhibits the same temperature ranges (400–500 °C) (Fig. 11). Quartz related to the W–Sn mineralization stage of veins is characterized by colder crystallization temperatures between 350 and 450 °C. These crystallization temperatures are compatible with those described in greisen systems worldwide (Smith *et al.*, 1996; Conliffe and Feely, 2006; Audétat *et al.*, 2008) and with temperatures obtained from fluid inclusions and boron isotopes exchange thermometry for the earliest hydrothermal stages of veins (Kelly and Rye, 1979; Bussink, 1984; Noronha *et al.*, 1992; Lüders, 1996; Codeço *et al.*, 2019). Finally, temperatures depict a cooling trend from magmatic quartz of granite to hydrothermal quartz of greisen and veins. This cooling trend is consistent with the expected thermic evolution of magmatic-hydrothermal systems and suggests a continual transition between magmatic and hydrothermal processes (i.e greisenization and W–Sn-bearing quartz veins).

## 9.4 Spatiotemporal connection between the granite emplacement, greisenization and ore-bearing quartz veins

Experimental and empirical studies have demonstrated that the closure temperature of apatite range from 375 to 550 °C (Chamberlain and Bowring, 2001; Schoene and Bowring, 2006; Cochran *et al.*, 2014). Consequently, U–Pb dating of apatite represents a good tool to constrain ages of cooling for large and polyphased intrusive bodies. However, Pochon *et al.* (2016) have demonstrated that the closure temperature of apatite is much higher (770 to 870 °C) in the case of small intrusive bodies such as dyke and sill because their cooling rate is then very fast. In such cases, U–Pb dating of apatite can be

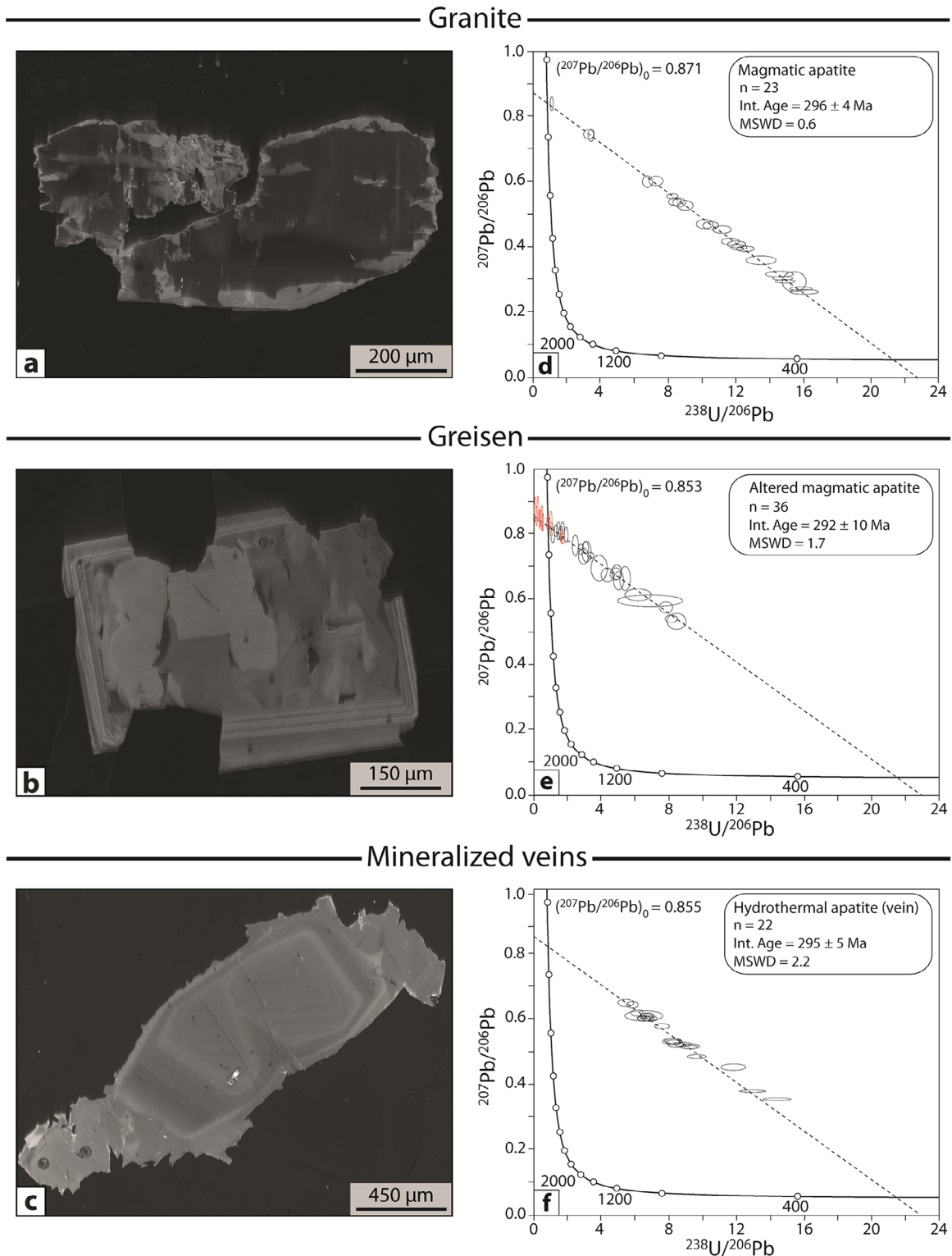


**Fig. 10.** (a) to (c) Representative cathodoluminescence images of (a) magmatic apatite from two mica granite, (b) altered magmatic apatite from greisen and (c) hydrothermal apatite from mineralized vein selvages. (d) to (e) Tera–Wasserburg concordia diagrams, in which apatite analyses were reported to define lower intercept date. (d) Results obtained for magmatic apatite from the unaltered two-mica granite. (e) Results obtained for altered magmatic apatite from greisen. Black ellipses correspond to analyses of altered magmatic apatite and red ellipses correspond to hydrothermal oscillatory zoning overgrowths (f) Results obtained for hydrothermal apatite from the mineralized veins (veins selvages). The black dashed lines represent the unforced discordias used for age determination, the  $(^{207}\text{Pb}/^{206}\text{Pb})_0$  values obtained from the upper intersect of discordias are also indicated. Ellipses and errors on ages are reported at  $2\sigma$ .

used to date the emplacement age of these magmatic rocks. In addition, apatite is highly reactive during fluid–rock interactions (Harlov *et al.*, 2005; Bouzari *et al.*, 2016; Ballouard *et al.*, 2018) and hence constitutes a good proxy to date hydrothermal events and metasomatic processes related to greisenization.

The gravity survey performed by Ribeiro (2017) showed that the Panasqueira two-mica granite is a small laccolith of 7.5 x 4.5 km in plan view with a thickness less than 2 km. Accordingly, the cooling rate of the Panasqueira granite was likely high. Therefore, the U–Pb age of  $296 \pm 4$  Ma obtained in this study on magmatic apatite can be interpreted as the emplacement age of the Panasqueira two-mica granite. This emplacement age overlaps the formation of the vein selvages, dated at  $295 \pm 5$  Ma (U–Pb dating of hydrothermal apatite, this study) and  $296 \pm 0.6$  Ma (Ar–Ar dating of muscovite-rich selvages, Snee *et al.*, 1988). The U–Pb apatite age ( $292 \pm 10$  Ma) for greisenization is within errors identical to ages obtained for veins and granite cooling. Accordingly, greisenization and formation of W–Sn-bearing quartz veins of were coeval with the emplacement and the crystallization of the Panasqueira two-mica granite. Furthermore, hydrothermal activity related to the sulfides mineralization of the veins dated at  $294 \pm 0.9$  Ma (by Ar–Ar dating of late muscovite, Snee *et al.*, 1988) appears to be contemporaneous with both the granite emplacement and the W–Sn mineralization stage. Consequently, the different hydrothermal stages observed in mineralized veins of Panasqueira were related to the same thermal event, which was likely controlled by the emplacement and the crystallization of the granitic intrusion. The overlap between the ages of the granite emplacement, greisenization and the formation of the W–Sn mineralized quartz veins, in combination with their strong spatial relationships suggest that the Panasqueira granite and the W–Sn-bearing quartz veins are genetically linked. Additionally, the occurrences of disseminated cassiterite and scarce wolframite in the greisen, as well as the greisen enrichment in ore metals (W and Sn) compared to the Panasqueira granite support the interpretation that greisenization was coeval with vein formation and resulted from the ingress of W–Sn-rich fluids through the apical part of the granitic intrusion.

### 9.5 Evidences for magmatic fluid exsolution

Hydrothermal white-mica from greisen and ore-bearing quartz veins are enriched in fluid mobile granophile elements (F, Li, Rb, Cs, Sn and W) suggesting involvement of magmatic contributions. Alkali metal (Li, Rb and Cs) are commonly used as differentiation proxies for pegmatite and W–Sn mineralized vein systems (Neiva, 1987; Černý *et al.*, 2005; Hulsbosch *et al.*, 2014). During fractional crystallization, these incompatible elements get enriched in the residual granitic melt and then in the orthomagmatic fluids exsolved during the final consolidation of the granitic intrusion. Although white-mica from greisen and veins are hydrothermal in origin, their compositions define a linear trend with magmatic muscovite in  $\log(K/Rb)$  versus  $\log(Cs)$  diagram (Fig. 12a). Hulsbosch *et al.* (2014) interpret this linear relationship as a result of Rayleigh fractional crystallization process in magmatic-hydrothermal systems. At Panasqueira, this relationship seems to confirm

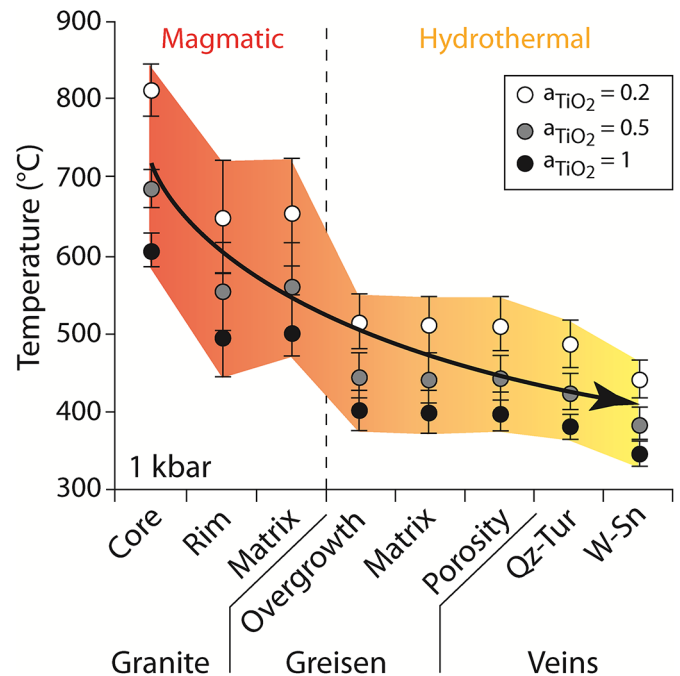


**Fig. 11.** Temperatures of quartz crystallization obtained for the different generations of magmatic and hydrothermal quartz of the unaltered two-mica granite, greisen and mineralized veins. Temperatures were obtained by applying the TitaniQ geothermometer defined by Thomas *et al.* (2010) at 1 kbar for Ti activity ranging from 0.2 to 1.

that white-mica from the greisen and the W–Sn bearing quartz veins both crystallized from magmatic fluids, which were equilibrated with residual granitic melt during the final stage of magmatic–hydrothermal crystallization of granite. Compositions of magmatic and hydrothermal white-mica appear to be consistent with the theoretical compositional evolution trend predict by Rayleigh fractional crystallisation model of the Panasqueira granite (blue dashed line in Fig. 12b). This supports the interpretation that fractional crystallization of the Panasqueira granite is the most likely process for the production of fluids enriched in the granophile elements found in hydrothermal white-mica. Both greisenization and formation of W–Sn-bearing veins resulted from the exsolution of acidic magmatic W–Sn bearing fluids during the magmatic-hydrothermal transition, which marks the final stage of fractional crystallization of the Panasqueira granite. The focusing of ore-bearing fluids by the cupola determined by Launay *et al.* (2018) at the magmatic-hydrothermal transition, as well as the magmatic boron isotopic composition of tourmalines from veins realized by Codeço *et al.* (2017, 2019) support this interpretation.

### 9.6 Genetic relationship between the greisenization and the W–Sn mineralization

As highlighted from (i) temperature evolution constrained from quartz geothermometry, (ii) geochemical signature of fluids deduced from quartz and white-mica compositions and (iii) U–Pb apatite geochronology, greisenization and the formation of the mineralized veins were coeval and resulted

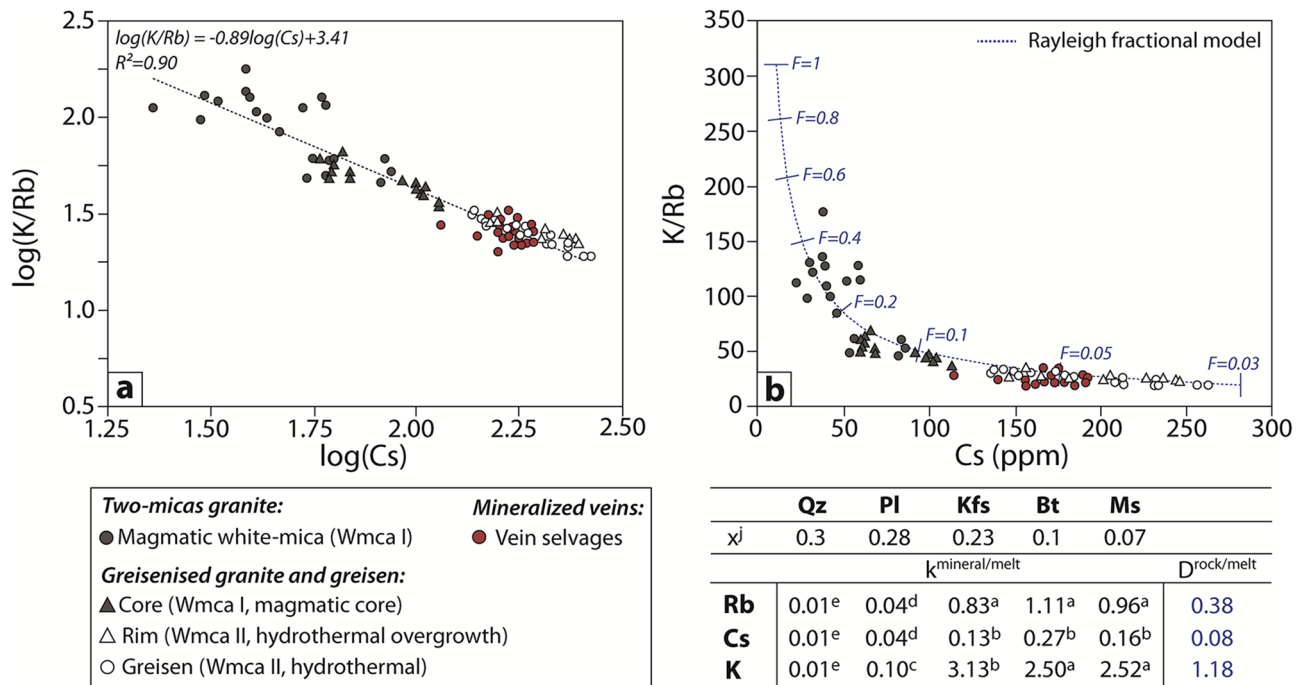


**Fig. 12.** (a)  $\log(K/Rb)$  versus  $\log(Cs)$  relationship in white-mica composing granite, greisen and the mineralized veins of Panasqueira. (b) Modelled compositional evolution trend of white-mica formed during fractional crystallization of the Panasqueira granite ( $F$  gives the fraction of remaining liquid). This trend is calculated applying the Rayleigh equation  $C_i^{Ms} = k_{di}^{Ms/melt} * C_{0,i}^{Liq} * F^{(D_i-1)}$  (Hulsbosch *et al.*, 2014) and assuming a starting composition of granitic melt ( $C_{0,i}^{Liq}$ ) of 370 ppm Rb, 70 ppm Cs and 44 900 ppm K. Modal proportion of minerals ( $x^j$ ) composing the Panasqueira two-mica granite and mineral/melt partition coefficients ( $k_{d,i}^j$ ) for K, Rb and Cs used for calculation of distribution coefficients ( $D_i$ ) are summarized in table below diagram (b). References for  $k_d$ : <sup>a</sup>Icenhower and London (1996); <sup>b</sup>Icenhower and London (1995); <sup>c</sup>Philpotts and Schnetzler (1970); <sup>d</sup>Jolliff *et al.* (1992); <sup>e</sup>Nash and Crecraft (1985).

likely from the exsolution of orthomagmatic W–Sn-bearing fluids. The coeval formation of wolframite-bearing veins and greisen was already demonstrated by Korges *et al.* (2018) for the Zinnwald Sn–W deposit, by Monnier *et al.* (2018, 2020) for the Echassières district, and by Chen *et al.* (2019, 2020) for the Maoping deposit. According to these studies Sn-greisen formation and precipitation of quartz–Sn–W veins result from the exsolution of a single magmatic-hydrothermal fluid released during the progressive cooling of the deeper granitic intrusion. To illustrate the interaction between fluids produced during the late stage of fractional crystallization of the Panasqueira granite and greisenization, a conceptual model based on the disequilibrium between hot acidic magmatic fluids released at high temperature and cooler crystallized part of the granite intrusion is proposed (Fig. 13). If we consider that albite, k-feldspar and muscovite are equilibrated during the final stages of the granite crystallization (eutectic), the composition of magmatic fluids in  $\log(a_{Na^+}/a_{H^+})$  and  $\log(a_{K^+}/a_{H^+})$  released by the granite is constrained by the triple point at high temperature conditions (red star at 600 °C in Fig. 13d). The exsolution and the circulation of these fluids through the cooler and crystallized part of the intrusive body trigger the replacement of feldspars by muscovite due to disequilibrium caused by the temperature differences between hot-acidic magmatic fluids (600 °C in Fig. 13d) and crystallized granite (400 °C). During the hydrolysis of feldspars and biotite, white-mica and quartz

recorded the chemical signature of fluids that were enriched in granophile elements and metals, whereas elements hosted by feldspars (Ca, Na, Ba, Sr...) were released in fluids (Fig. 13b). The crystallization of a large amount of white-mica and quartz and chemical exchanges between these minerals and fluids explain the overall Cs, Rb, Li enrichment and Na, Ba and Sr depletion observed in greisen. Reactions of feldspar replacement in quartz–white mica assemblage neutralized the acidity of mineralized fluids. This fluid neutralization can induce a Sn solubility decrease and thus precipitation of cassiterite (Heinrich, 1990; Migdisov and Williams-Jones, 2005; Schmidt, 2018). This may explain the occurrences of cassiterite in the greisen porosity. As, the W–Sn bearing fluids flowed through the vein network during the earliest mineralization stages (QTS and MOSS) that triggered the opening and the formation of the mineralized veins (Foxford *et al.*, 2000; Launay *et al.*, 2018). In these veins, the white-mica-rich selvages and quartz recorded the same fluid chemical signatures than the quartz–white mica assemblage composing the greisen. As highlighted by Lecumberri-Sanchez *et al.* (2017) from whole rock and fluid inclusion analyses, interactions between these W–Sn-bearing fluids and metasedimentary host rocks caused strong alteration along vein margins (Fig. 13c) (tourmalinization and muscovitization). These intense fluid–rock interactions triggered Fe leaching from schist and hence crystallization of wolframite in mineralized veins.

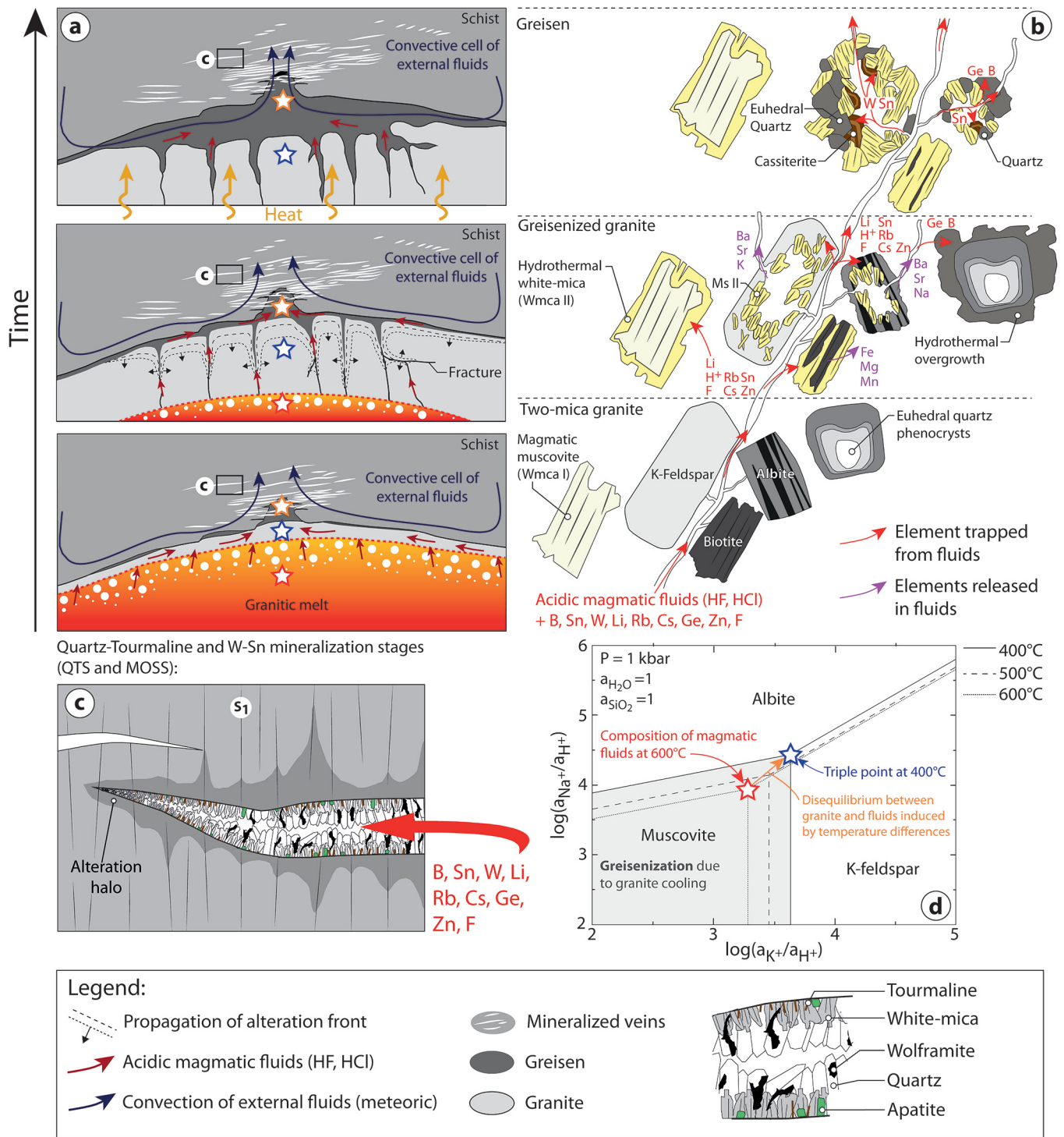


**Fig. 13.** Conceptual model of greisen formation during the magmatic-hydrothermal transition of Panasqueira. In this model are displayed (a) the schematic time evolution of fluid flow during the granite crystallization and cooling, (b) the textural and the mineralogical evolution of granite with the behavior of some elements considered in this study, (c) zoom on mineralized veins related to QTS and MOSS and (d)  $\log(a_{Na^+}/a_{H^+})$  vs.  $\log(a_{K^+}/a_{H^+})$  phases diagram at 1 kbar illustrating effect of temperatures (from 600 to 400 °C) on equilibria between K-feldspar, albite and muscovite. Triple point corresponds to hypothetical eutectic of the two-mica granite of Panasqueira. During granite cooling, fluid produced at high magmatic temperature (red star) is imbalance with the cooler crystallized part of the granite intrusion that potentially trigger greisenization. This diagram was built from thermodynamic database of SUPCRTBL (Johnson *et al.*, 1992; Zimmer *et al.*, 2016).

## Supplementary Material

Supplementary Material: [ESM1–ESM8](#).

The Supplementary Material is available at <http://www.bsgf.fr/10.1051/bsgf/2020046/olm>.

**Acknowledgments.** We thank Dr. Ross Sherlock for his careful proofreading and language corrections. This research took part in the ERAMIN project “New Ores” (ANR-14-EMIN-0001) and was financially supported by the French Geological Survey (BRGM), the Region Centre, and the Labex Voltaire (ANR-10-LABX-100-01).

## References

- Ackerson M, Mysen BO, Tailby N, Watson E. 2018. Low-temperature crystallization of granites and the implications for crustal magmatism. *Nature* 559. <https://doi.org/10.1038/s41586-018-0264-2>.
- Alfonso P, Melgarejo JC, Yusta I, Velasco F. 2003. Geochemistry of feldspars and muscovite in granitic pegmatite from the Cap de Creus field, Catalonia, Spain. *The Canadian Mineralogist* 41: 103–116.
- Anderson MJ. 2001. A new method for non-parametric multivariate analysis of variance. *Austral Ecology* 26: 32–46.
- Audétat A, Pettke T, Heinrich CA, Bodnar RJ. 2008. Magmatic-hydrothermal evolution in a fractionating granite: a microchemical study of the Sn-W-F mineralized Mole granite (Australia). *Geochim Cosmochim Acta* 64: 3373–3393.
- Azor A, Dias da Silva Í, Gómez Barreiro J, González-Clavijo E, Martínez Catalán JR, Simancas JF, *et al.* 2019. Deformation and structure. In: Quesada C, Oliveira JT, eds. *The Geology of Iberia: A Geodynamic Approach: Vol. 2: The Variscan Cycle, Regional Geology Reviews*. Cham: Springer International Publishing, pp. 307–348. [https://doi.org/10.1007/978-3-030-10519-8\\_10](https://doi.org/10.1007/978-3-030-10519-8_10).
- Ballouard C, Poujol M, Mercadier J, Deloule E, Boulvais P, Baele JM, *et al.* 2018. Uranium metallogenesis of the peraluminous leucogranite from the Pontivy-Rostrenen magmatic complex (French Armorican Variscan belt): the result of long-term oxidized hydrothermal alteration during strike-slip deformation. *Mineralium Deposita* 53: 601–628.
- Belissant R, Boiron MC, Luais B, Cathelineau M. 2014. LA-ICP-MS analyses of minor and trace elements and bulk Ge isotopes in zoned Ge-rich sphalerites from the Noailhac-Saint-Salvy deposit (France): insights into incorporation mechanisms and ore deposition processes. *Geochim. Cosmochim. Ac.* 126: 518–540.
- Bishop AC. 1989. Greisen. In: *Petrology. Encyclopedia of Earth Science*. Boston, MA: Springer.
- Bouzzari F, Hart CJR, Bissig T, Barker S. 2016. Hydrothermal alteration revealed by apatite luminescence and chemistry: a potential indicator mineral for exploring covered porphyry copper deposits. *Economic Geology* 111: 1397–1410.
- Breiter K, Müller A, Leichmann J, Gabašová A. 2005. Textural and chemical evolution of a fractionated granitic system: the Podleší stock, Czech Republic. *Lithos* 80: 323–345.
- Breiter K, Svojtka M, Ackerman L, Švecová K. 2012. Trace element composition of quartz from the Variscan Altenberg-Teplička caldera (Krušné hory/Erzgebirge Mts, Czech Republic/Germany): insights into the volcano-plutonic complex evolution. *Chem. Geol.* 326–327: 36–50.
- Breiter K, Ďurišová J, Dosbaba M. 2017a. Quartz chemistry – A step to understanding magmatic-hydrothermal processes in ore-bearing granites: Činovec/Zinnwald Sn-W-Li deposit, Central Europe. *Ore Geology Reviews* 90: 25–35.
- Breiter K, Ďurišová J, Hrstka T, Korbelová Z, Vanková MH, Galiova MV, *et al.* 2017b. Assessment of magmatic vs. metasomatic processes in rare-metal granites: a case study of the Činovec/Zinnwald Sn–W–Li deposit, Central Europe. *Lithos* 292: 198–217.
- Breiter K, Hložková M, Korbelová Z, Vasinova Galiova M. 2019. Diversity of lithium mica compositions in mineralized granite–greisen system: Činovec Li–Sn–W deposit, Erzgebirge. *Ore Geology Reviews* 106. <https://doi.org/10.1016/j.oregeorev.2019.01.013>.
- Bussink RW. 1984. Geochemistry of the Panasqueira Tungsten-Tin Deposit, Portugal. *Geol. Ultraiectina*.
- Carocci E, Marignac C, Cathelineau M, Truche L, Lecomte A, Pinto F. 2018. Rutile from Panasqueira (Central Portugal): An Excellent Pathfinder for Wolframite Deposition. *Minerals* 9: 9. <https://doi.org/10.3390/min9010009>.
- Carocci E, Marignac C, Cathelineau M, Truche L, Poujol M, Boiron M, *et al.* 2020. Incipient wolframite deposition at Panasqueira (Portugal): W-rutile and tourmaline compositions as proxies for early fluid composition. *Economic Geology*.
- Castro A, Corretgé GL, De La Rosa J, Enrique P, Martínez FJ, Pascual E, *et al.* 2002. Palaeozoic Magmatism. In: Gibbons W, Moreno MT, eds. *The Geology of Spain*. London: Geological Society, pp. 117–53.
- Černý P, Blevin PL, Cuney M, London D. 2005. Granite-Related Ore Deposits. In: Hedenquist JW, Thompson JFH, Goldfarb RJ, Richards JR, eds. *Economic Geology – One Hundredth Anniversary Volume*, pp. 337–370.
- Chamberlain KR, Bowring SA. 2001. Apatite-feldspar U–Pb thermochronometer: a reliable, mid-range (~450 °C), diffusion controlled system. *Chemical Geology* 172: 173–200.
- Chen LL, Ni P, Dai BZ, Li WS, Chi Z, Pan JY. 2019. The genetic association between quartz vein-and greisen-type mineralization at the maoping W–Sn deposit, southern Jiangxi, China: insights from zircon and cassiterite U–Pb ages and cassiterite trace element composition. *Minerals* 9(7): 411.
- Chen G, Gao J, Lu J, Zhang R. 2020. In situ LA-ICP-MS analyses of mica and wolframite from the Maoping tungsten deposit, southern Jiangxi, China. *Acta Geochimica*, 1–19.
- Chew DM, Petrus JA, Kamber BS. 2014. U–Pb LA-ICPMS dating using accessory mineral standards with variable common Pb. *Chemical Geology* 363: 185–199.
- Clark AH. 1964. Preliminary study of the temperatures and confining pressures of granite emplacement and mineralization, Panasqueira, Portugal. *Inst. Mining Metall. Trans.* 73: 813–824.
- Cochrane R, Spikings RA, Chew D, Wotzlaw JF, Chiaradia M, Tyrrell S, *et al.* 2014. High temperature (> 350 °C) thermochronology and mechanisms of Pb loss in apatite. *Geochimica et Cosmochimica Acta* 127: 39–56.
- Codeço M, Weis P, Trumbull R, Pinto F, Lecumberri-Sanchez P, Wilke F. 2017. Chemical and boron isotopic composition of hydrothermal tourmaline from the Panasqueira W–Sn–Cu deposit, Panasqueira W–Sn–Cu deposit, Portugal. *Chemical Geology* 468: 1–16. <https://doi.org/10.1016/j.chemgeo.2017.07.011>.
- Codeço MS, Weis P, Trumbull RB, Glodny J, Wiedenbeck M, Romer RL. 2019. Boron-isotope muscovite-tourmaline geothermometry indicates fluid cooling during magmatic-hydrothermal W–Sn-ore formation. *Economic Geology* 114(1): 153–163. <https://doi.org/10.5382/econgeo.2019.4625>.
- Codeço MS, Weis P, Trumbull RB, Van Hinsberg V, Pinto F, Lecumberri-Sanchez P, *et al.* 2020. The imprint of hydrothermal fluids on trace-element contents in white mica and tourmaline from the Panasqueira W–Sn–Cu deposit, Portugal. *Mineralium Deposita*.
- Conliffe J, Feely M. 2006. Microthermometrics characteristics of fluids associated with granite and greisen quartz and vein quartz

- and beryl from Rosses Granite complex, Donegal, NW Ireland. *J Geochem Explor* 89: 73–77.
- Dias G, Letierri J, Mendes A, Simões P, Bertrand JM. 1998. U-Pb zircon and monazite geochronology of syn- to post-tectonic Hercynian granitoids from the central Iberian Zone (northern Portugal). *Lithos* 45: 349–369.
- Dolejs D. 2015. Quantitative characterization of hydrothermal systems and reconstruction of fluid fluxes: the significance of advection, disequilibrium, and dispersion. In: *SGA Proceedings 13th SGA Biennial Meeting*.
- Dostal J, Kontak DJ, Ochir G, Shellnutt J, Fayek M. 2015. Cretaceous ongonites (topaz-bearing albite-rich microleucogranites) from Ongon Khairkhan, Central Mongolia: Products of extreme magmatic fractionation and pervasive metasomatic fluid: Rock interaction. *Lithos* 236-237: 173–189.
- Foxford KA, Nicholson R, Polya DA. 1991. Textural evolution of W–Cu–Sn bearing hydrothermal quartz veins at Minas da Panasqueira, Portugal. *Mineralogical Magazine* 55: 435–445.
- Foxford KA, Nicholson R, Polya DA, Hebblethwaite RPB. 2000. Extensional failure and hydraulic valving at Minas da Panasqueira, Portugal: Evidence from vein spatial distributions, displacements and geometries. *J. Struct. Geol.* 22: 1065–1086.
- Gomes M, Neiva A. 2000. Chemical zoning of muscovite from the Ervedosa granite, northern Portugal. *Mineralogical Magazine* 64: 347–358. <https://doi.org/10.1180/002646100549247>.
- Götze J, Plötze M, Graupner T, Hallbauer DK, Bray CJ. 2004. Trace element incorporation into quartz: a combined study by ICP-MS, electron spin resonance, cathodoluminescence, capillary ion analysis, and gas chromatography 1. *Geochimica et Cosmochimica Acta* 68: 3741–3759.
- Grant JA. 1986. The isocon diagram; a simple solution to Gresens' equation for metasomatic alteration. *Economic Geology* 81(8): 1976–1982.
- Guidotti CV. 1984. Micas in metamorphic rocks. In: Bailey SW, ed. *Micas*. Washington: Mineralogical Society of America, pp. 357–467.
- Gurbanov AG, Chernukha DG, Koshchug DG, Kurasova SP, Fedyushchenko SV. 1999. EPR spectroscopy and geochemistry of rock-forming quartz as an indicator of the superimposed processes in rocks of igneous associations of various ages in the Greater Caucasus. *Geochem. Int.* 37: 519–604.
- Halter WE, Williams-Jones AE, Kontak DJ. 1996. The role of greisenization in cassiterite precipitation at the East Kemptville tin deposit, Nova Scotia. *Economic Geology* 91(2): 368–385.
- Harlov DE, Wirth R, Förster HJ. 2005. An experimental study of dissolution-reprecipitation in fluorapatite: fluid infiltration and the formation of monazite. *Contrib Mineral Petr* 150: 268–286.
- Heaney PJ, Veblen DR, Post JE. 1994. Structural disparities between chalcedony and macrocrystalline quartz. *American Mineralogist* 79: 452–460.
- Hebblethwaite RPB, Antao AM. 1982. A report on the study of dilation patterns within the Panasqueira ore body: Barroca Grande, Beralta Tin Wolfram (Portugal), unpub. rept., 15 p.
- Heinrich CA. 1990. The chemistry of hydrothermal tin-tungsten ore deposits. *Econ. Geol.* 85: 457–481.
- Huang R, Audétat A. 2012. The titanium-in-quartz (Titanium) thermometer: a critical examination and re-calibration. *Geochimica et Cosmochimica Acta* 84: 75–89.
- Hulsbosch N, Hertogen J, Dewaele S, André L, Muchez P. 2014. Alkali metal and rare earth element evolution of rock-forming minerals from the Gatumba area pegmatites (Rwanda): quantitative assessment of crystal-melt fractionation in the regional zonation of pegmatite groups. *Geochim. Cosmochim. Acta* 132: 349–374.
- Icenhower J, London D. 1995. An experimental study of element partitioning among biotite, muscovite, and coexisting peraluminous silicic melt at 200 MPa (H<sub>2</sub>O). *Am. Mineral.* 80: 1229–1251.
- Icenhower J, London D. 1996. Experimental partitioning of Rb, Cs, Sr, and Ba between alkali feldspar and peraluminous melt. *Am. Mineral.* 81: 719–734.
- Jacamon F, Larsen RB. 2009. Trace element evolution of quartz in the charnockitic Kleivan granite, SW-Norway: the Ge/Ti ratio of quartz as an index of igneous differentiation. *Lithos* 107: 281–291.
- Johnson JW, Oelkers EH, Helgeson HC. 1992. SUPCRT92-A software package for calculating the standard molal thermodynamic properties of minerals, gases, aqueous species, and reactions from 1-bar to 5000-bar and 0°C to 1000°C. *Computer and Geosciences* 18: 899–947.
- Jolliff BL, Papike JJ, Shearer CK. 1992. Petrogenetic relationships between pegmatite and granite based on geochemistry of muscovite in pegmatite wall zones, Black Hills, South Dakota, USA. *Geochim. Cosmochim. Acta* 56: 1915–1939.
- Julivert M, Fontboté JM, Ribeiro A, Conde L. 1972. Mapa Tectónico de la Península Ibérica y Baleares E. 1:1 000 000. *Inst. Geol. Min., España, Madrid*.
- Kaeter D, Barros R, Menuge J, Chew D. 2018. The magmatic–hydrothermal transition in rare-element pegmatites from southeast Ireland: LA-ICP-MS chemical mapping of muscovite and columbite–tantallite. *Geochimica et Cosmochimica Acta*. 240. <https://doi.org/10.1016/j.gca.2018.08.024>.
- Kelly WC, Rye RO. 1979. Geologic, fluid inclusion and stable isotope studies of the tin-tungsten deposits of Panasqueira, Portugal. *Econ Geol* 74: 1721–1822.
- Korges M, Weis P, Lüders V, Laurent O. 2018. Depressurization and boiling of a single magmatic fluid as a mechanism for tin-tungsten deposit formation. *Geology* 46(1): 75–78.
- Kotlyar BB, Ludington S, Mosier DL. 1995. Descriptive, grade, and tonnage models for molybdenum-tungsten greisen deposits: U.S. Geological Survey, Open-File Report 95-584, 30 p.
- Larsen RB, Henderson H, Ihlen PM, Jacamon F. 2004. Distribution and petrogenetic behaviour of trace elements in granitic pegmatite quartz from granite from South Norway. *Contributions to Mineralogy and Petrology* 147: 615–628.
- Launay G, Sizaret S, Guillou-Frottier L, Gloaguen E, Pinto F. 2018. Deciphering fluid flow at the magmatic-hydrothermal transition: A case study from the world-class Panasqueira W-Sn-(Cu) ore deposit (Portugal). *Earth and Planetary Science Letters* 499: 1–12.
- Launay G. 2019. Dynamic permeability related to greisenization in Sn–W ore deposits: Quantitative petrophysical and experimental evidence. *Geofluids*. <https://doi.org/10.1155/2019/5976545>.
- Lecumberri-Sanchez P, Vieira R, Heinrich CA, Pinto F, Wälle M. 2017. Fluid-rock interaction is decisive for the formation of tungsten deposits. *Geology* 45: 579–582.
- Legros H, Marignac C, Mercadier J, Cuney M, Richard A, Wang R-C, et al. 2016. Detailed paragenesis and Li-mica compositions as recorders of the magmatic-hydrothermal evolution of the Maoping W–Sn deposit (Jiangxi, China). *Lithos* 264: 108–124.
- Legros H, Marignac C, Tabary T, Mercadier J, Richard A, Cuney M, et al. 2018. The ore-forming magmatic-hydrothermal system of the Piaotang W–Sn deposit (Jiangxi, China) as seen from Li-mica geochemistry. *American Mineralogist*. 103: 39–54. <https://doi.org/10.2138/am-2018-6196>.
- Lehmann B. 1990. Lehmann Metallogeny of tin. In: *Lecture notes in Earth Sciences* 32, Springer-Verlag, 211 p.
- London D, Hervig RL, Morgan GB. 1988. Melt-vapor solubilities and elemental partitioning in peraluminous granite-pegmatite systems:

- experimental results with Macusani glass at 200 MPa. *Contrib. Mineral. Petrol.* 99: 360–373.
- Lüders V. 1996. Contribution of infrared microscopy to fluid inclusion studies in some opaque minerals (Wolframite, Stibnite, Bournonite): Metallogenic implications. *Economic Geology* 91(8): 1462–1468.
- Ludwig KR. 2012. User's Manual for Isoplot 3.75. A geochronological toolkit for Microsoft Excel. Berkeley Geochronological Center, pp. 1–75.
- Luth WC, Jahns RH, Tuttle OF. 1964. The granite system at pressures of 4 to 10 kilobars. *J. Geophys. Res.* 69(4): 759–773. <https://doi.org/10.1029/JZ069i004p00759>.
- Mao Z, Cheng Y, Liu J, Yuan S, Wu S, Xiang X, *et al.* 2013. Geology and molybdenite Re–Os age of the Dahutang granite-related veinlets-disseminated tungsten ore field in the Jiangxin Province, China. *Ore Geology Reviews* 53: 422–433.
- Marignac C, Cuney M, Cathelineau M, Lecomte A, Carocci E, Pinto F. 2020. The Panasqueira rare metal granite suites and their involvement in the genesis of the world-class Panasqueira W–Sn–Cu vein deposit: a petrographic, mineralogical, and geochemical study. *Minerals* 10(6): 562.
- Martins I, Mateus A, Figueiras J, Rodrigues P, Pinto F. 2020. Thermal evolution of the W–Sn(–Cu) Panasqueira ore system (Portugal): insights from pyrite-pyrrhotite and arsenopyrite geothermometers. *Comunicações Geológicas*.
- Mateus A, Figueiras J, Martins I, Rodrigues PC, Pinto F. 2020. Relative abundance and compositional variation of silicates, oxides and phosphates in the W–Sn-rich lodes of the Panasqueira mine (Portugal): implications for the ore-forming process. *Minerals* 10 (6): 551.
- McDowell FW, McIntosh WC, Farley KA. 2005. A precise  $^{40}\text{Ar}$ – $^{39}\text{Ar}$  reference age for the Durango apatite (U–Th)/He and fission-track dating standard. *Chemical Geology* 214: 249–263.
- Michaud J, Gumiaux C, Pichavant M, Gloaguen E, Marcoux E. 2020. From magmatic to hydrothermal Sn–Li–(Nb–Ta–W) mineralization: The Argemela area (central Portugal). *Ore Geology Reviews* 116: 103215. <https://doi.org/10.1016/j.oregeorev.2019.103215>.
- Migdisov AA, Williams-Jones AE. 2005. An experimental study of cassiterite solubility in HCl-bearing water vapour at temperatures up to 350 °C. Implications for tin ore formation. *Chemical Geology* 217: 29–40.
- Miller CF, Stoddard EF, Bradfish LJ, Dollase WA. 1981. Composition of plutonic muscovite: genetic implications. *Can. Mineral.* 19: 25–34.
- Monecke T, Kempe U, Götze J. 2002. Genetic significance of the trace element content in metamorphic and hydrothermal quartz: a reconnaissance study. *Earth and Planetary Science Letters* 202: 709–724.
- Monier G, Merggoil-Daniel J, Labernardière H. 1984. Générations successives de muscovites et feldspaths potassiques dans les leucogranites du massif de Millevaches (Massif Central Français). *Bull. Mineral.* 107: 55–68.
- Monier G, Robert J-L. 1986. Evolution of the miscibility gap between muscovite and biotite solid solutions with increasing lithium content: an experimental study in the system  $\text{K}_2\text{O}$ – $\text{Li}_2\text{O}$ – $\text{MgO}$ – $\text{FeO}$ – $\text{Al}_2\text{O}_3$ – $\text{SiO}_2$ – $\text{H}_2\text{O}$ – $\text{HF}$  at 600 °C, 2 kbar  $\text{PH}_2\text{O}$ : comparison with natural lithium micas. *Mineralogical Magazine* 50: 641–651.
- Monnier L, Lach P, Salvi S, Melleton J, Bailly L, Béziat D, *et al.* 2018. Quartz trace-element composition by LA-ICP-MS as proxy for granite differentiation, hydrothermal episodes, and related mineralization: The Beauvoir Granite (Echassières district), France. *Lithos* 320–321: 355–377.
- Monnier L, Salvi S, Melleton J, Bailly L, Béziat D, Parseval P, *et al.* 2019. Multiple generations of wolframite mineralization in the Echassières District (Massif Central, France). *Minerals* 9: 637. <https://doi.org/10.3390/min9100637>.
- Monnier L, Salvi S, Jourdan V, Sall S, Bailly L, Melleton J, *et al.* 2020. Contrasting fluid behavior during two styles of greisen alteration leading to distinct wolframite mineralizations: the Echassières district (Massif Central, France). *Ore Geology Reviews*, 103648.
- Młynarczyk M, Sherlock R, Williams-Jones A. 2002. San Rafael, Peru: Geology and structure of the worlds richest tin lode. *Mineralium Deposita* 38: 555–567.
- Müller A, Kronz A, Breiter K. 2002. Trace elements and growth patterns in quartz: a fingerprint of the evolution of the subvolcanic Podlesí Granite System (Krušné Hory, Czech Republic). *Bulletin of the Czech Geological Survey* 77: 135–145.
- Müller A, van den Kerkhof AM, Behr H-J, Kronz A, Koch-Müller M. 2010. The evolution of late-Hercynian granites and rhyolites documented by quartz – A review. *Geol. Soc. Am. Spec. Pap.* 472: 185–204.
- Müller A, Herklotz G, Giegling H. 2018. Chemistry of quartz related to the Zinnwald/Cínovec Sn–W–Li greisen-type deposit, Eastern Erzgebirge, Germany. *Journal of Geochemical Exploration* 190: 357–373.
- Nash WP, Crecraft HR. 1985. Partition coefficients for trace elements in silicic magmas. *Geochimica et Cosmochimica Acta* 49: 2309–2322.
- Neiva AMR. 1987. Geochemistry of greisenized granites and metasomatic schists of tungsten-tin deposits in Portugal. In: Helgeson HC, ed. *Chemical Transport in Metasomatic Processes*. NATO ASI Series C218, pp. 681–700.
- Neiva AMR, Silva MMVG, Gomes MEP. 2007. Crystal chemistry of tourmaline from Variscan granites, associated tin-tungsten- and gold deposits, and associated metamorphic and metasomatic rocks from northern Portugal. *Neues Jahrbuch für Mineralogie – Abhandlungen* 184(1): 45–76.
- Noronha F, Doria A, Dubessy J, Charoy B. 1992. Characterization and timing of the different types of fluids present in the barren and ore-veins of the W–Sn deposit of Panasqueira, Central Portugal. *Mineralium Deposita* 27: 72–79. <https://doi.org/10.1007/BF00196084>.
- Paton C, Woodhead JD, Hellstrom JC, Hergt JM, Greig A, Maas R. 2010. Improved laser ablation U–Pb zircon geochronology through robust downhole fractionation correction. *Geochemistry, Geophysics, Geosystems* 11.
- Pearce N, Perkins W, Westgate J, Gorton M, Jackson S, Neal C, Chenery S. 1997. A compilation of new and published major and trace element data for NIST SRM 610 and NIST SRM 612 glass reference materials. *Geostandards and Geoanalytical Research* 21: 115–144. <https://doi.org/10.1111/j.1751-908X.1997.tb00538.x>.
- Philpotts JA, Schnetzler CC. 1970. Phenocryst-matrix partition coefficients for K, Rb, Sr and Ba, with applications to anorthosite and basalt genesis. *Geochimica et Cosmochimica Acta* 34: 307–322.
- Pichavant M. 1981. An experimental study of the effect of boron on a water-saturated haplogranite at 1 kbar vapour pressure. *Contributions to Mineralogy and Petrology* 76: 430–439.
- Pichavant M, Villaros A, Deveaud S, Scaillet B, Lahlafi M. 2016. The influence of redox state on mica crystallization in leucogranitic and pegmatitic liquids. *The Canadian Mineralogist* 54: 559–581. <https://doi.org/10.3749/canmin.1500079>.
- Pirajno F. 1992. Greisen systems. In: *Hydrothermal Mineral Deposits*. Berlin, Heidelberg: Springer, pp. 280–324.

- Pirajno F. 2009. Hydrothermal processes and mineral systems. Dordrecht: Springer.
- Pochon A, Poujol M, Gloaguen E, Branquet Y, Cagnard F, Gumiaux C, *et al.* 2016. U–Pb LA-ICP-MS dating of apatite in mafic rocks: evidence for a major magmatic event at the Devonian-Carboniferous boundary in the Armorican Massif (France). *Am. Mineral.* 101: 2430–2442.
- Pollard PJ, Taylor RG, Cuff C. 1988. Genetic Modelling of Greisen-Style Tin Systems. In: Hutchison CS, ed. *Geology of Tin Deposits in Asia and the Pacific*. Berlin, Heidelberg: Springer, pp 59–72.
- Polya DA. 1989. Chemistry of the main-stage ore-forming fluids of the Panasqueira W–Cu–(Ag)–Sn deposit, Portugal: implications for models of ore genesis. *Econ. Geol.* 84: 1134–1152.
- Polya DA, Foxford KA, Stuart F, Boyce A, Fallick AE. 2000. Evolution and paragenetic context of low  $\delta D$  hydrothermal fluids from the Panasqueira W–Sn deposit, Portugal: New evidence from microthermometric, stable isotope, noble gas and halogen analyses of primary fluid inclusions. *Geochim. Cosmochim. Acta* 64: 3357–3371.
- Ribeiro RF. 2017. Gravimetric Modelling and Geological Interpretation of Argemela-Panasqueira Area. Unpublished MSc thesis, Universidade do Porto.
- Robb L. 2005. Introduction to ore-forming processes. Malden, MA: Blackwell Publishing, 373 p.
- Rusk B. 2012. Cathodoluminescent textures and trace elements in hydrothermal quartz. In Götz J, Möckel R, eds. *Quartz: Deposits, Mineralogy and Analytics*. Heidelberg, New York: Springer, pp. 307–329.
- Rusk B, Reed M. 2002. Scanning electron microscope-cathodoluminescence analysis of quartz reveals complex growth histories in veins from the Butte porphyry copper deposit, Montana. *Geology* 30(8): 727–730.
- Sanderson DJ, Roberts S, Gumiel P, Greenfield C. 2008. Quantitative Analysis of Tin- and Tungsten-Bearing Sheeted Vein Systems. *Economic Geology* 103: 1043–1056. <https://doi.org/10.2113/gsecongeo.103.5.1043>.
- Schmidt C. 2018. Formation of hydrothermal tin deposits: Raman spectroscopic evidence for an important role of aqueous Sn(IV) species. *Geochimica et Cosmochimica Acta* 220: 499–511.
- Schoene B, Bowring SA. 2006. U–Pb systematics of the McClure Mountain syenite: Thermochronological constraints on the age of the  $^{40}\text{Ar}/^{39}\text{Ar}$  standard MMhb. *Contributions to Mineralogy and Petrology* 151: 615–630.
- Smith MP, Banks DA, Yardley BWD. 1996. Fluid inclusion and stable isotope constraints on the genesis of the Cligga Head Sn–W deposit, SW England. *Eur J Mineral* 8: 961–974.
- Snee LW, Sutter JF, Kelly WC. 1988. Thermochronology of economic mineral deposits; dating the stages of mineralization at Panasqueira, Portugal, by highprecision  $^{40}\text{Ar}/^{39}\text{Ar}$  age spectrum techniques on muscovite. *Econ Geol* 83: 335–354.
- Speer JA. 1984. Micas in igneous rocks. In: Bailey SW, ed. *Micas. Reviews in Mineralogy*, Vol. 13. Washington D.C.: Mineralogical Society of America, pp. 299–356.
- Stacey JS, Kramer JD. 1975. Approximation of terrestrial lead isotope evolution by a two stage model. *Earth Planetary Sciences Letters* 26: 207–221.
- Stemprok M. 1987. Greisenization (a review). *Geologische Rundschau*, Springer-Verlag 76: 169–175.
- Stemprok M, Pivec E, Langrova A. 2005. The petrogenesis of a wolframitebearing greisen in the Vykmanov granite stock, Western Krušné hory pluton (Czech Republic). *Bulletin of Geosciences* 80 (3): 163–184.
- Taylor RG. 1979. Geology of tin deposits. *Developments in Economic Geology, Elsevier*, 11: 543.
- Taylor RG, Pollard PJ. 1988. Pervasive hydrothermal alteration in tin-bearing granite and implications for the evolution of ore-bearing magmatic fluids. *Canadian Institute of Mining and Metallurgy Special* 39: 86–95.
- Thadeu D. 1951. Geologia do couto mineiro da Panasqueira. *Comunic Serv Geol Port* 32: 5–64.
- Thomas JB, Watson EB, Spear FS, Shemella PT, Nayak SK, Lanzirrotti A. 2010. Titanite under pressure: the effect of pressure and temperature on the solubility of Ti in quartz. *Contributions to Mineralogy and Petrology* 160: 743–759.
- Tischendorf G, Gottesmann B, Förster H.-J., Trumbull RB. 1997. On Li-bearing micas: estimating Li from electron microprobe analyses and an improved diagram for graphical representation. *Mineral. Mag.* 61: 809–834. <https://doi.org/10.1180/minmag.1997.061.409.05>.
- Tuttle OF, Bowen NL. 1958. Origin of granite in the light of experimental studies in the system  $\text{NaAlSi}_3\text{O}_8\text{--KAlSi}_3\text{O}_8\text{--SiO}_2\text{--H}_2\text{O}$ . *Geological Society of America*. <https://doi.org/10.1130/MEM74>.
- Van Daele J, Hulbosch N, Dewaele S, Boiron MC, Piessens K, Boyce A. 2018. Mixing of magmatic-hydrothermal and metamorphic fluids and the origin of peribatholithic Sn vein-type deposits in Rwanda. *Ore Geology Reviews*. 101. <https://doi.org/10.1016/j.oregeorev.2018.07.020>.
- Vilas L, de San Jose MA, Garcia-Hidalgo JF, Herranz P, Pelaez JR, Perejon A, *et al.* 1990. Autochthonous Sequences. In: Dallmeyer RD, Garcia EM, eds. *Pre-Mesozoic Geology of Iberia, IGCP-Project 233*. Berlin, Heidelberg: Springer, pp. 145–219. [https://doi.org/10.1007/978-3-642-83980-1\\_14](https://doi.org/10.1007/978-3-642-83980-1_14).
- Villaseca C, Merino E, Oyarzun R, Orejana D, Pérez-Soba C, Chicharro E. 2014. Contrasting chemical and isotopic signatures from Neoproterozoic metasedimentary rocks in the Central Iberian Zone (Spain) of pre-Variscan Europe: Implications for terrane analysis and Early Ordovician magmatic belts. *Precambrian Research* 245: 131–145. <https://doi.org/10.1016/j.precamres.2014.02.006>.
- Wark DA, Watson EB. 2006. Titanite: a titanium-in-quartz geothermometer. *Contributions to Mineralogy and Petrology* 152: 743–754.
- Weil JA. 1984. A review of electron spin spectroscopy and its application to the study of paramagnetic defects in crystalline quartz. *Physics and Chemistry of Minerals* 10: 149–165.
- Werner ABT, Sinclair WD, Amey EB. 2014. International strategic mineral issues summary report–Tungsten (ver. 1.1, November 2014). U.S. Geological Survey Circular 930-O, 74 p.
- Wheeler A. 2015. Technical report on the mineral resources and reserves of the Panasqueira mine, Portugal. Report NI 43-101, Prepared for Almonty Industries.
- Whitney DL, Evans BW. 2010. Abbreviations for names of rock-forming minerals. *Am. Mineral* 95: 185–187.
- Williamson BJ, Stanley CJ, Wilkinson JJ. 1997. Implications from inclusions in topaz for greisenisation and mineralisation in the Hensbarrow topaz granite, Cornwall, England. *Contributions to Mineralogy and Petrology* 127(1-2): 119–128.
- Winderbaum L, Ciobanu CL, Cook NJ, Paul M, Metcalfe A, Gilbert S. 2012. Multivariate analysis of an LA-ICP-MS trace element dataset for pyrite. *Math. Geosci.* 44: 823–842.
- Yokart B, Barr SM, Williams-Jones AE, Macdonald AS. 2003. Late-stage alteration and tin-tungsten mineralization in the Khuntan Batholith, northern Thailand. *Journal of Asian Earth Sciences* 21 (9): 999–1018.

- Zhao WW, Zhou MF, Li YHM, Zhao Z, Gao JF. 2017. Genetic types, mineralization styles, and geodynamic settings of Mesozoic tungsten deposits in South China. *Journal of Asian Earth Sciences* 137: 109–140.
- Zheng Z, Chen YJ, Deng XH, Yue SW, Chen HJ, Wang QF. 2018. Fluid evolution of the Qiman Tagh W-Sn ore belt, East Kunlun Orogen, NW China. *Ore Geology Reviews* 95: 280–291.
- Zimmer K, Zhang YL, Lu P, Chen YY, Zhang GR, Dalkilic M, *et al.* 2016. SUPCRTBL: A revised and extended thermodynamic dataset and software package of SUPCRT92. *Computer and Geosciences* 90: 97–111.

**Cite this article as:** Launay G, Sizaret S, Lach P, Melleton J, Gloaguen E, Poujol M. 2021. Genetic relationship between greisenization and Sn–W mineralization in vein and greisen deposits: Insights from the Panasqueira deposit (Portugal), *BSGF - Earth Sciences Bulletin* 192: 2.